catalysts

MDPI

Article

Styrene Oxidation to Valuable Compounds over Nanosized FeCo-Based Catalysts: Effect of the Third Metal Addition

Ana Paula Saraiva Oliveira [1], Igor Santos Gomes [1], Alcineia Conceição Oliveira [1,*], Josue Mendes Filho [2], Gilberto Dantas Saraiva [2,3], João Maria Soares [4], Francisco Ferreira de Sousa [2,5] and Adriana Campos [6]

1 Departamento de Química Analítica e Físico-Química, Campus do Pici, Bloco 940, Universidade Federal do Ceará, Fortaleza 60455-760, Brazil; n_eia@yahoo.com (A.P.S.O.); igor.santos.gomes_12@hotmail.com (I.S.G.)
2 Departamento de Física, Campus do Pici-Bloco 922, Universidade Federal do Ceará, Fortaleza 60455-760, Brazil; josue@fisica.ufc.br (J.M.F.); gilberto@fisica.ufc.br (G.D.S.); francisco_ferreira@fisica.ufc.br (F.F.d.S.)
3 Faculdade de Educação Ciências e Letras do Sertão Central, Universidade Estadual do Ceará, Quixadá/CE 63900-000, Brasil
4 Universidade do Estado do Rio Grande do Norte, BR 110-km 48, Mossoró 59625-620, Brazil; joaosoares@gmail.com
5 Campus Universitário de Marabá, Universidade Federal do Sul e Sudeste do Pará, Marabá 68505-080, Para, Brazil
6 Centro de Tecnologias Estratégicas do Nordeste-CETENE, Av. Prof. Luiz Freire, 1, Cidade Universitária, Recife 50740-540, Brazil; adriana.cetene@gmail.com
* Correspondence: alcineia@ufc.br; Tel./Fax: +55-853-366-9008

Academic Editors: Tian-Yi Ma, Jian-Rong (Jeff) Li and Cláudia Gomes Silva
Received: 3 September 2017; Accepted: 23 October 2017; Published: 30 October 2017

Abstract: Nanosized FeCo-based solids were prepared via distinct preparation procedures. The catalytic performances of the solids for styrene oxidation in the presence of hydrogen peroxide were evaluated. The addition of promoters in FeCo such as Sn, Mo, or Cu was also investigated. The catalysts were characterized with XRD, Raman spectroscopy, TEM, chemical analyses, EPR and SEM-EDS. Of these solids obtained via four different methods, the catalyst prepared via the NC and CM procedures enabled a partial incorporation of the Sn into the FeCo matrix forming a very active phase, namely the Heusler alloy. This was ascribed to the high initial dispersion of Sn as a promoter into the FeCo matrix, which led to available FeCoSn (FCS) particles well dispersed and stable on the catalyst surface. In the case of incorporating Mo or Cu to the nanosized FeCo catalyst, a poor stability towards leaching was observed when operating under the same reaction conditions. Cu was much less active than both Sn and Mo, mainly leading to acetophenone, ethylbenzene, 2-phenyl ethanol, 2-phenyl acetic acid, and 2-phenyl acetaldehyde products. The best catalytic results under the optimized reaction conditions, especially at 50 °C and styrene/H_2O_2 molar ratio of 1 were achieved with nanosized FCS. This solid had a conversion of ca. 70% and selectivity for aldehydes of ca. 27%, and the selectivity for the condensation products was 29%.

Keywords: styrene oxidation; ternary oxides; FeCo catalyst; nanosized; preparation method

1. Introduction

Fe-based solids are one of the most widely studied catalytic materials in converting hydrocarbons through oxidation reactions, owing to their promising physicochemical properties [1–3]. The features

of these materials including redox ability, pronounced stability at moderate temperatures, reusability, relatively high textural properties, and low cost make these materials affordable for applications in catalysis, adsorption, dyes degradation, metals and toxic gases removal [1–4].

Over the past several years, various preparation routes have been developed to Fe-based catalysts such as incipient wetness impregnation [4], core-shell [5], sol–gel [6–8], soft-template or hard-template methods [9,10], decomposition of Fe salts in the presence of hydrocarbons followed by thermal treatments and solvothermal routes [4,11] and mechanosynthesis [12], among others. However, some of the reported preparation methods often require an expensive apparatus, long reaction times, and, sometimes, additional steps to prepare the materials.

Currently, the high-surface-area Fe-based nanometer-sized and nanostructured materials have become the focus of considerable interest due to their unique properties, when applied in catalysis [5,8,9]. More importantly, these types of materials are the choice for most Fe-supported and unsupported catalysts due to low-cost fabrication and mass availability of the solids. Among these methods, the sol–gel route to prepare iron compounds has been verified to be a relatively simple and efficient process of fabricating diverse Fe-containing phases for hydrocarbon oxidations [12]. As an example, the particle size and porosity of the nanoparticles and nanostructures can be controlled using the alkoxides precursors, and this fact is presumably related to the dissolution of the precursors and reactions involved in the process [8].

In this sense, massic or supported Fe oxide nanoparticles have widespread applications in selective epoxidation of olefins, alkenes, and alcohols [4,13,14]. Within this field, styrene oxidation is an allylic oxidation reaction to produce valuable chemical compounds such as styrene epoxide and benzaldehyde (Figure 1, Reaction I).

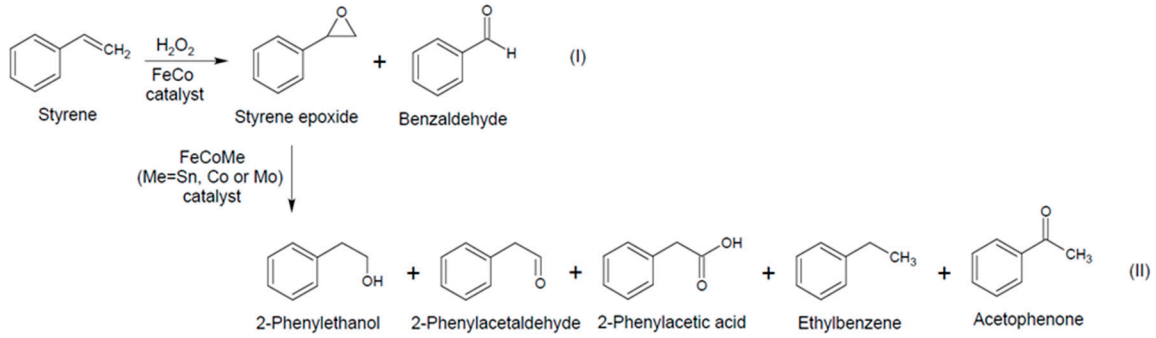

Reaction II is another pathway for styrene oxidation reaction leading to the formation of valuable chemical products such as 2-phenylehtnol, 2-phenyl acetic acid, 2-phenyl acetaldehyde, acetophenone, and ethylbenzene. These products have wide applications in the manufacture of perfumes, dyestuff, pharmaceuticals, and agrochemicals and in organic synthesis [12,15]. The use of FeCo-based catalysts in Reaction I has become an area of growing interest, since the solids exhibit promising catalytic activity and can be easily isolated from the reaction products [16,17]. On the contrary, they present the possibility of deactivation via phase transformation, sintering, or leaching of the active phases occurring during the reaction [12]. It has also been shown that the addition of promoters (i.e., Te, Mn, Mo, Sb, Co, or V) to Fe-based catalysts, particularly Co, is a great approach to have reoxidation couples and hence provide a redox stabilization of Fe oxidation states to enhance selectivities of desired products [17,18].

Herein, a series of ternary FeCo catalysts with different promoters (Sn, Cu, or Mo) have been synthesized via nanocasting, sol–gel, chemical modification, and copolymer-assisted co-precipitation. The resulting materials essentially may suppress the deactivation of Fe^{3+} via reduction during Reaction I through the immediate proximity of the promoter in the lattice of a given Fe catalytically active phase. This has been investigated via EPR, XRD, Raman spectroscopy, Nitrogen physisorption isotherms, chemical analysis, SEM-EDS, and TEM measurements. Further, the challenging aspect is to choose a facile preparation method to synthesize FeCo materials with the promoter incorporated into the

FeCo lattice without agglomeration. With a low cost-effective method, the simple synergistic strategy of addition of the promoter would result in a versatile FeCo catalyst. This has rarely been exploited beyond styrene oxidation.

2. Results and Discussion

2.1. Physicochemical Properties of the Synthesized Solids

The morphology of the material is of utmost importance for designing catalysts for oxidation reactions [12,15]. SEM images of the FCS series of solids are illustrated in the panels (Figure 1a). The chemical modification procedure, e.g., CM, promotes the formation of particles comprised of truncated rombicuboctahedron, prismatic, trapezoidal, and parallelogram-shaped morphologies, which are indeed quite large agglomerates with uneven surfaces. Moreover, the particle sizes of FCS CM are not uniform with the mean crystal domain of 1–50 µm. The magnified view of an individual parallelogram (Figure 1a included, left side) exhibits plate facets in the dense crystals, as a result of the aminobenzoic acid, furfural, or iso-octil phenoxy poly-ethoxi ethanol precursor decomposition. The hydrocarbon precursors may be chemically bonded to the ferrocene, tin, and cobalt salts acting as binders to provide stability to the final solid. As reported in an earlier study [19], the thermal treatment of samples prepared via similar methods in air at 700 °C gives a solid state reaction among Fe-O, Co-O, and C-O as well as Co-O and Sn-O entities; hence, the crystallization of the FCS CM sample is likely. The crystallization of the solid is later reflected in the XRD and Raman.

It is interesting to note that the cabbage-leaf-like particles are clearly seen over FCS SG (Figure 1a), and some of them have nanochip- and nanosphere-aggregated forms (Figure 1a included, left side). In addition to the porous network structure formed by the aggregate of nanoscale particles, the particles are nanostructured.

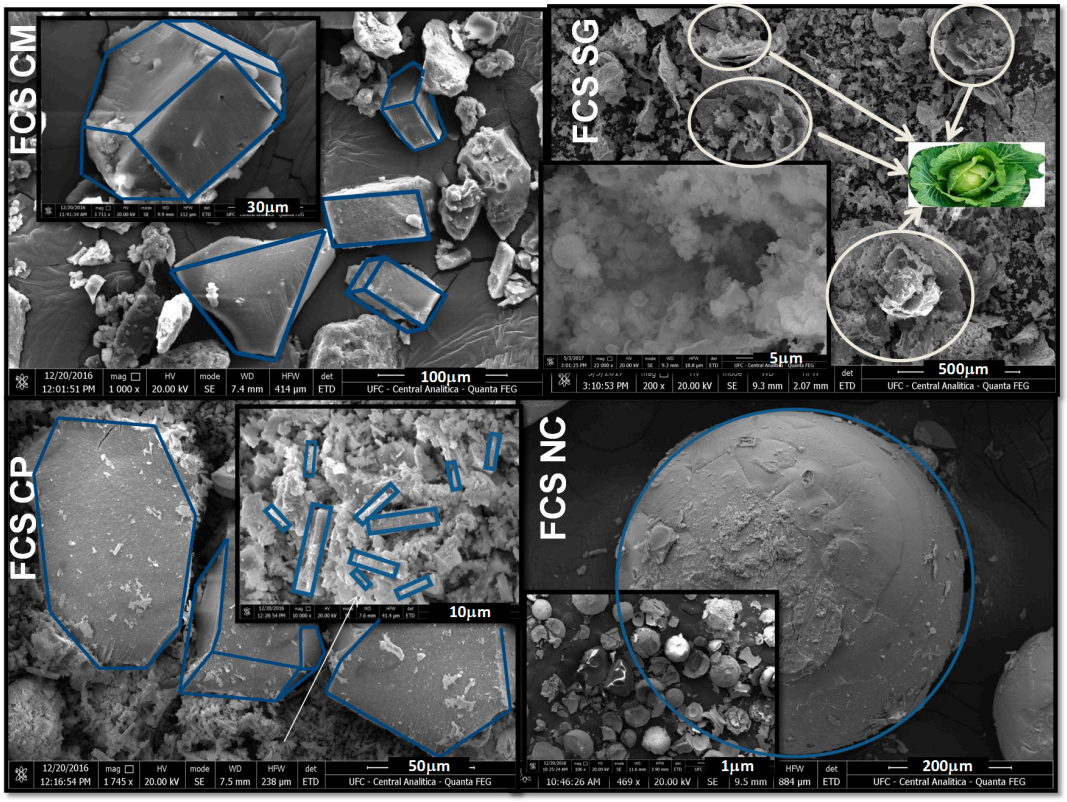

(**a**)

Figure 1. *cont.*

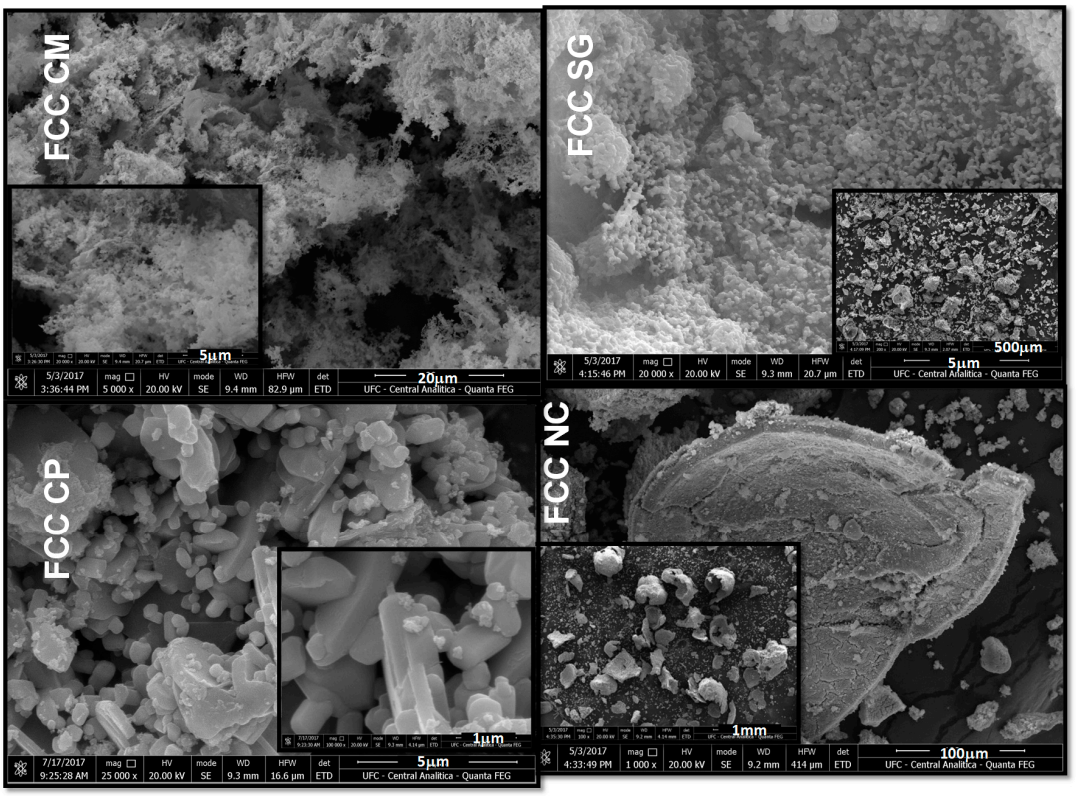

(**b**)

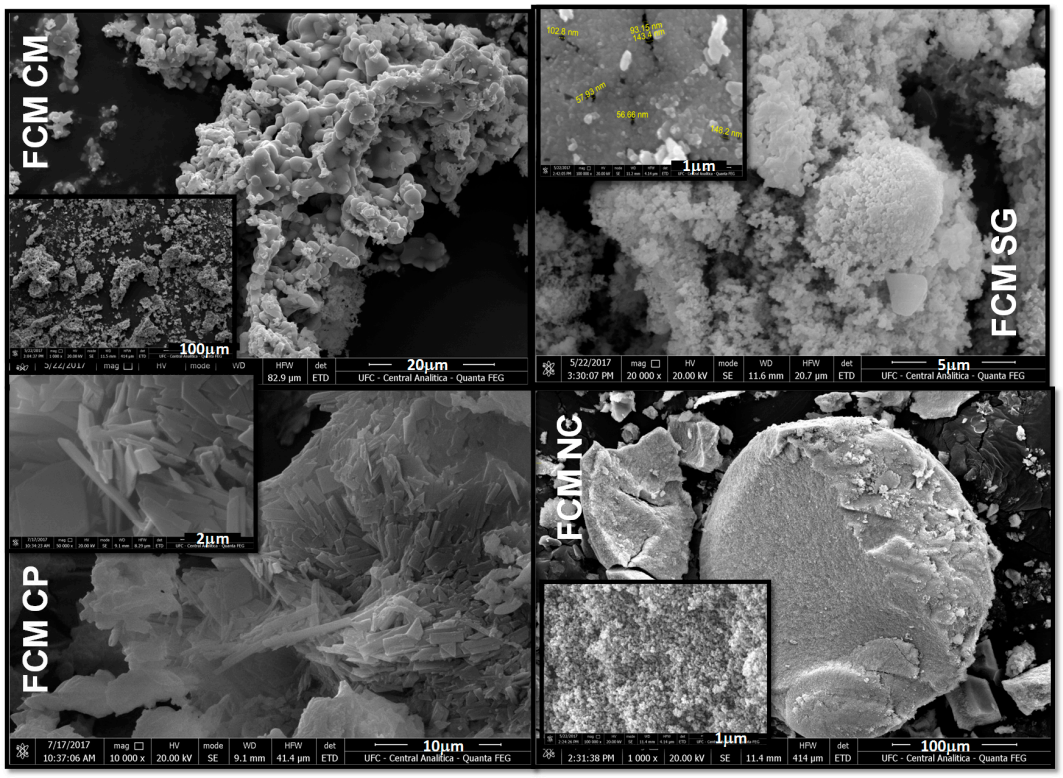

(**c**)

Figure 1. *cont.*

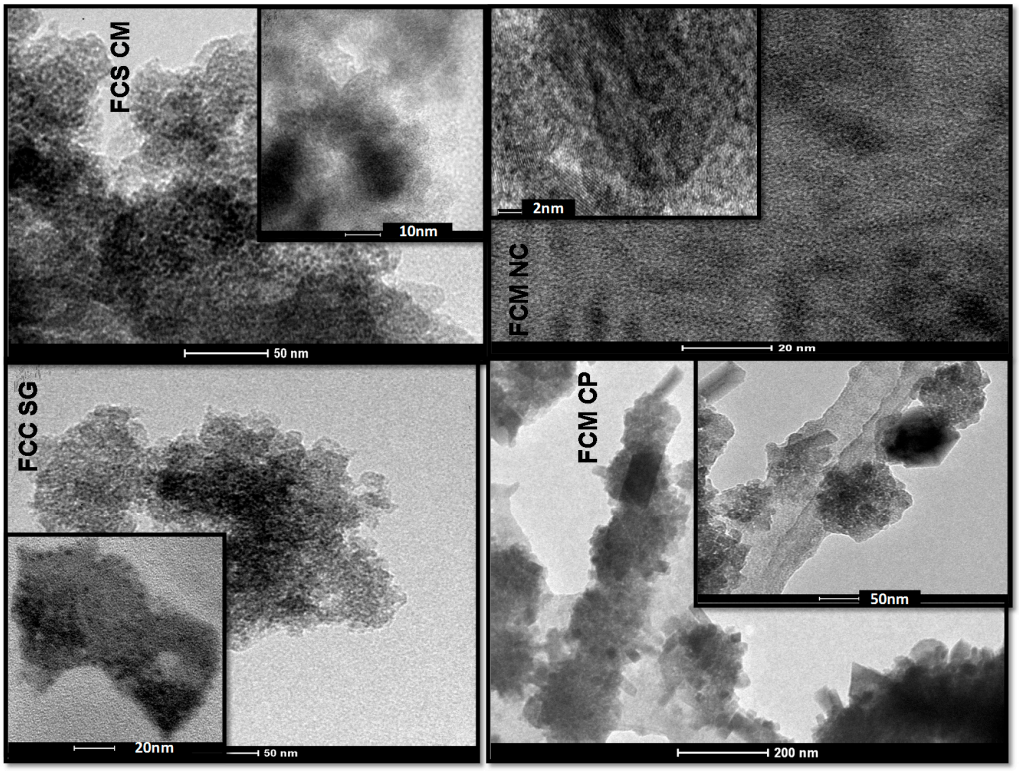

(**d**)

Figure 1. SEM images of the solids studied: (**a**) FCS series, (**b**) FCC series and (**c**) FCM series. (**d**) TEM images of the FCS CM, FCM NC, FCC SG and FCM CP samples. The included images in SEM and TEM panels correspond to the magnified images of the samples.

The SEM micrograph of FCS CP exhibits a rod-like morphology with rods or ribbons shapes (Figure 1a included, right side), and the diameter of the platelet is in the 3–10 μm range. It is interesting to observe an evident presence of particles possessing roughly flat hexagonal plates morphology along with prismatic and cuboctahedron shapes, mostly aggregated with no well-known morphologies. These results might be due to the CP method as a variant of sol–gel method, providing the interactions among the depolimerized P-123 copolymer, hydrochloric acid, citric acid, and the metal precursors. It can provide an anisotropic aggregation of thermodynamically unstable metal–oxo–metal or metal–hydroxy–metal species, all of them giving a void space of self-assembled micellar, as for Fe-based compounds [20,21]. In addition, the sol–gel involved reactions are occurring simultaneously during the aging step [21]. Further, hydrothermal treatment and calcination steps would result in the formation of nanosized particles with poor crystallinity (XRD and Raman results), leading to samples with a peculiar morphology.

The FCS NC depicted egg-shaped spheres featuring a particular morphology with rough particles covering the sphere (Figure 1a). This nanoarchitecture is duly reflected by the XAD-16 resin template hollow sphere morphology [20,21]. Some of the spheres were unbroken, indicating that the metal precursors infiltrated successfully into the spheres, whilst other spheroids were cracked because the calcination process burned the template (Figure 1a included, left side). Aside from the morphology, particles diameters varied from 0.5 to 100 μm.

In the case of the FCC series, the morphologies were inherently related to the preparation method and the inclusion of Cu into the solid. For instance, FCC CM displayed bundles of fluffy particles (Figure 1b) with a globular geometric shape (Figure 1b included, left side). Contrary to expected, FCC NC series have distorted spheres, mostly being cracked, as observed in the side-view (Figure 1b, included). This result is indicative of a low quality of the ordered spheres with Cu addition due to the

collapse of the final solid, most probably during the calcination process. The FCC CP is composed of dense particles with a polyhedral shape morphology. Some of these particles formed a solid block of nanoplates with an uneven surface, in which rod and spherical nanoparticles cover the nanoplates (Figure 1b included, right side). The SEM image of FCC SG consists of marble-like nanoparticles (Figure 1b), formed by aggregated ultrathin nanosheets (Figure 1b included, left side).

Molybdenum addition in the solid developed a particular morphology in the FCM series with dependence on the procedure used to prepare the solids (Figure 1c). The FCM CM morphology consists of a braided hair-like shape with small aggregates of spheres distorted in the bean forms (Figure 1c included left side). It is remarkable that the FCM NC had a morphology similar to that of FCC NC (Figure 1b). Indeed, the surface of the sphere observed for FCM NC was almost broken and irregular with core permeated through the spheres walls (Figure 1c included on the left). This implies that the metal precursors penetrated into the core of the hollow spheres, and the subsequent thermal degradation contributed to the sintering process, in accordance with a previous work [20].

For FCM CP, numerous rods tangled together forming a big rough plate can be clearly seen. There were distinct rods attached with the plates possessing an average diameter of hundreds of nanometers, as can be observed in Figure 1c included on the left. The average length of such rods was found to be less than 5 μm. Interesting to note is that ice-cream-ball-like and pin-cushion morphologies were seen in FCM SG. Some voids were created among the nanoparticles by forming large pores, i.e., meso- and macropores of ca. 56–143 nm among the spaces of these nanoparticles (Figure 1c included, left side), as confirmed later via TEM image and physisorption measurements. Additionally, neither Cu nor Mo additions caused changes in the morphology of the SG samples; FCC SG and FCM SG samples retained their shape, as demonstrated in Figure 1b,c respectively. For a better explanation of this result, the surface tension of the liquid leads to the formation of nanoparticles with a spherical morphology and the formation of the aforesaid voids in sol–gel-based solids [8]. The morphology may indicate that the use of an organic polymer, such as polyvinylpyrrolidone in isopropyl alcohol together with citric acid and the metals, promotes the formation of a hydrogen bond between the amide carbonyl group of polymers and the metals, as for silica hybrid composites [22]. Consequently, ferrocene, cobalt, and the other metal precursors penetrated the polymer particles' pores such that nanocrystalline pores were formed, as for FCM SG (Figure 1c included, left side).

To further investigate the structure of the solids, TEM images were analyzed. Figure 1d depicts low-resolution TEM images of selected samples along with their corresponding high-resolution micrographs. The FCS CM sample contained a high number of irregularly shaped particles with any definite form. The magnified Figure 1d included indicates that the presence of tiny crystallites and large agglomerates. Both the tiny crystallites and large aggregates may be ascribed to Fe-based phases and Co nanoparticles. This supports the XRD pattern that revealed the formation of Fe-based phases, but did not show any Co nanoparticles due to the limitations of the XRD technique. Moreover, the average size of the nanoparticles, supposed to be from Co, was ca. 4 nm.

The FCC SG showed an agglomeration of particles representing a nanostructure with some small spherical nanoparticles confined within an agglomerate core. It is reasonable to believe that the co-polymer burning caused the coalescence of iron nanoparticles, which readily developed into a large agglomerate comprised of either Cu or Co nanoparticles. In addition, the diameters of the large particles were about 100 nm, indicating that the inner nanoparticles of ca. 10 nm were plainly embedded in the Fe nanostructure, which is consistent with the corresponding XRD and Raman results. Additionally, some voids that provoke pore formation were generated in the nanostructure, as later seen in textural properties analysis.

The formation of many nanorods and cubic crystals can be observed in FCM CP. It was revealed that the formation of these nanocrystals is a result of the crystallization of the iron precursor along with the carbonization of co-polymers and hydrocarbons on the metal surface to form a peculiar morphology [19]. Moreover, FCM NC displayed spherical particles, as shown by SEM images. Interestingly, the TEM image of FCM NC displayed aggregations of smaller particles, which stack

parallel to one another on the surface of the hard spheres. This is essentially characteristic of the metal deposition and growth of the particles on the solid surface [8].

These results confirm the SEM results that show the influence of the third metal addition on the morphology of the solid.

The chemical analyses via ICP-OES were performed to establish the metal concentrations of the samples. It should be mentioned that the presence of Fe, Co, and Sn constituted about 61.0, 19.5, and 19.5 wt % of the FCS samples (Table 1), independently of the preparation method.

These results suggest that the nominal concentration of Fe is very close to the one targeted in each synthesis, with the incorporation of approximately 65% of the desired Fe in the final solids. For the FCC and FCM series, the iron concentrations are 64 and 63 wt %, respectively. This is also very close to the targeted values. However, CP-based solids have their Co concentrations decreased in the FCC and FCM cases due to the leaching that impedes a complete incorporation of the Co into the Fe structure. Additionally, the concentrations of these metals in the CP method were the lowest among the samples studied. As a sound proof of the leaching of the elements during the washing and calcination steps, a dark liquid phase was formed during the calcination of the samples obtained via CP.

In agreement, the Fe/Me molar ratios (where Me = Sn, Cu, or Mo) are very close to that of the original molar ratio of 2. This indicates that the addition of Sn, Cu, or Mo to the reaction mixture containing Fe and Co precursors was successfully performed, being the third metal introduced into the FeCo solids. However, CP solids have the lowest Fe/Mo ratios among the solids studied. For instance, Fe/Mo of FCM CP is 1.3, and this is probably due to the leaching of Co species during synthesis, as above discussed.

To better understand the surface composition of the solids, EDS analyses were performed (Figure 2a). A visual inspection of the selected spectra reveals that the elements were well distributed on the solid surface.

Having recognized the peculiar morphology of the materials, it is useful to understand the actual textural properties of the solids. The textural parameters including surface areas, pore volumes, and pore sizes were examined through physisorption isotherms and pore diameters curves (Figure 2).

Nitrogen sorption isotherms of FCS series exhibit distinct isotherms (Figure 2b). Depending on the preparation method, one can see solids possessing Type IV isotherms with H_1 hysteresis and desorption occurring at 0.70 P/P_0 as for FCS CM, whereas an inflexion point occurring 0.47 P/P_0 with H_2 hysteresis loop is observable for FCS NC and FCS SG. In contrast, the FCS CP displayed features of a flat isotherm since the presence of synthesis debris has almost no hysteresis loop, which indicates that the sample has a small surface area. The pore size distribution curves (Figure 2c) exhibit a wide pore size possessing a non-uniform distribution for FCS NC and FCS SG. This could be an indication that the preparation method gives nanoparticles with uniform diameters and a smooth surface, as shown by sol–gel-derived samples [8]. In contrast to the other cases, FCS CP has a relatively sharp pore size distribution curve centered in the region of micropores.

Similar features with those of FCS are found on FCC and FCM series (Figure 2b). In other words, the Type IV isotherms with H_1 hysteresis are clearly observed for all synthesized samples, except for FCC CP and FCM CP having a Type I isotherm. Interestingly, FCC SG does not have a well-defined Type IV pattern, and this behavior corresponds to those of mesopores and macropores presence [20,21], as already suggested by SEM (Figure 1c included). Additionally, the hysteresis loop for the FCC SG is not well established, presumably because of the presence of inter-particle void space. On the contrary, the CP samples have a much narrower pore size distribution compared to FCC SG, indicating the presence of mesopores on the latter sample. Concerning the third metal presence, it can be noted that adding Mo or Cu does not significantly affect the formation of the nanosized materials obtained via sol–gel, as shown in Figure 1. Surprisingly, the diameter of particles became small due to the removal of some hydrocarbons during the calcined process, but no sintering of the solids was observed. In agreement, the EDS analysis reveals that the obtained samples only contained Fe, Co, Sn, Mo, or Cu elements with any residue of carbon, except for FCC CP sample (Figure 2a).

Table 1. Chemical composition of the solids from ICP-OES data. The textural properties of the solids synthesized by different methods through the data obtained from the nitrogen physisorption and pore distribution curves.

		ICP-OES Textural					Properties			
Series		**Fe (wt %)**	**Co (wt %)**	**Sn (wt %)**	**Cu (wt %)**	**Mo (wt %)**	**BET Surface Area (m^2 g^{-1})**	**t-Plot Micropore Area**	**Pore Volume (cm^3 g^{-1})**	**Pore Diameters (nm)**
FCS	NC	61.0	19.5	19.5 (1.9) [a]	-	-	45	0.3	0.18	15.6
	SG	60.2	19.8	20.0 (1.7) [a]	-	-	34	-	0.14	15.4
	CM	61.0	19.4	19.6 (1.8) [a]	-	-	24	-	0.10	6.1
	CP	62.3	18.8	18.9 (1.5) [a]	-	-	3	3	0.01	1.0
FCC	NC	64.0	18.0	-	17.0 (1.8) [b]	-	25	5	0.12	24.8
	SG	68.3	17.4	-	18.8 (1.8) [b]	-	12	-	0.07	16.2
	M	65.1	17.6	-	17.3 (1.7) [b]	-	11	0.4	0.06	16.9
	CP	64.7	16.8	-	18.5 (1.3) [b]	-	1	1	0.01	0.7
FCM	NC	63.5	18.5	-	-	18.0 (1.6) [c]	178	39	0.60	18.7
	SG	63.2	18.0	-	-	18.8 (1.7) [c]	35	7	0.13	10.8
	CM	63.7	18.2	-	-	18.1 (1.8) [c]	9	-	0.03	2.5
	CP	64.9	17.4	-	-	17.7 (1.3) [c]	2	2	0.01	1.0

[a] Fe/Sn molar ratios; [b] Fe/Cu molar ratios; [c] Fe/Mo molar ratios.

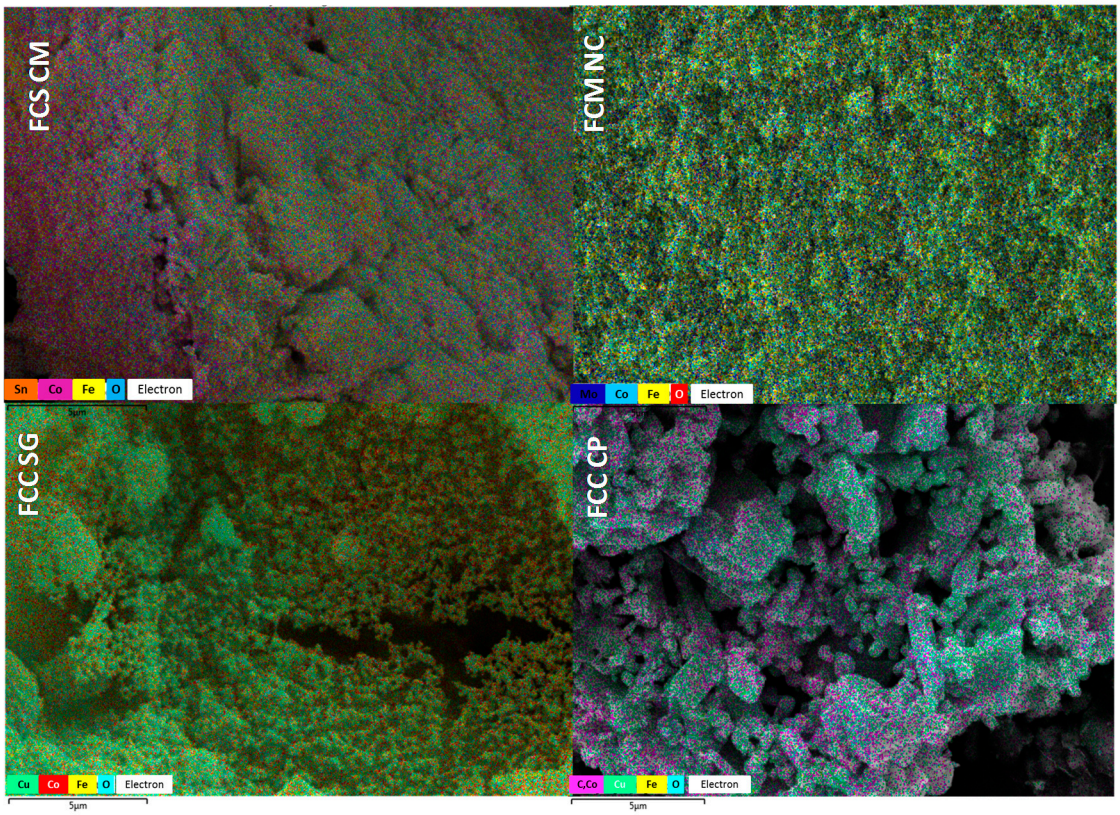

(**a**)

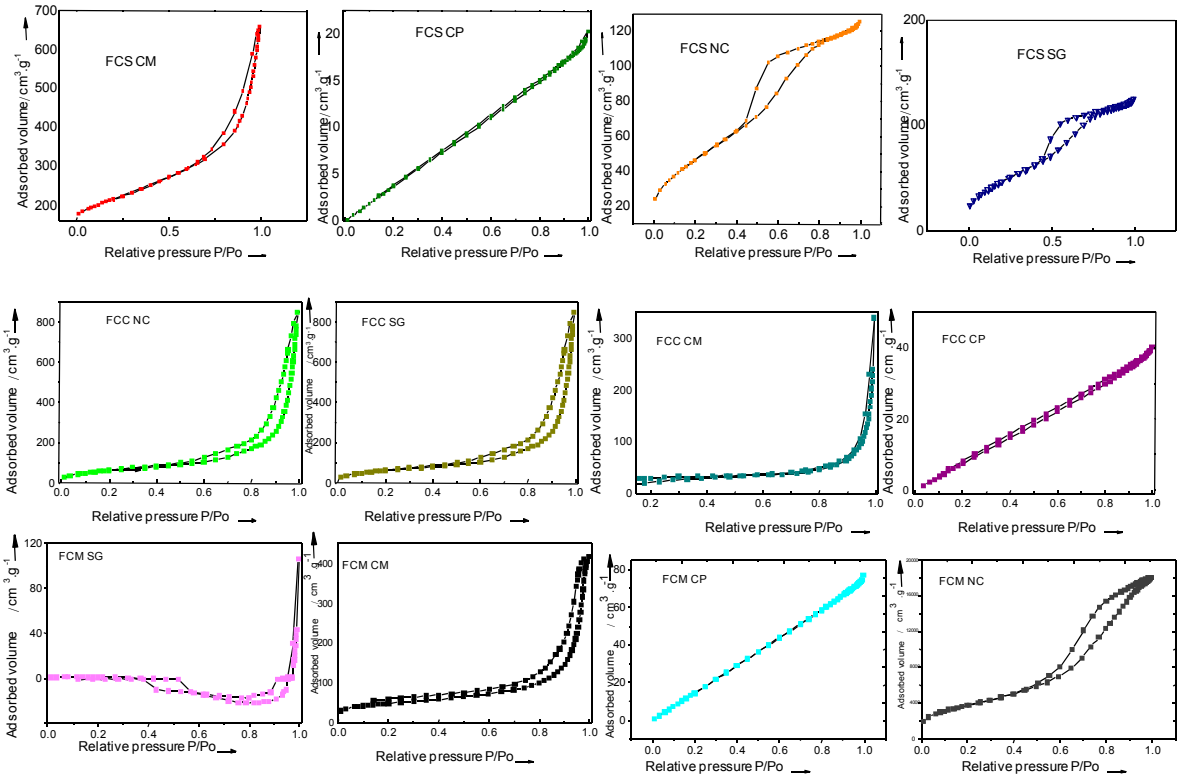

(**b**)

Figure 2. *cont.*

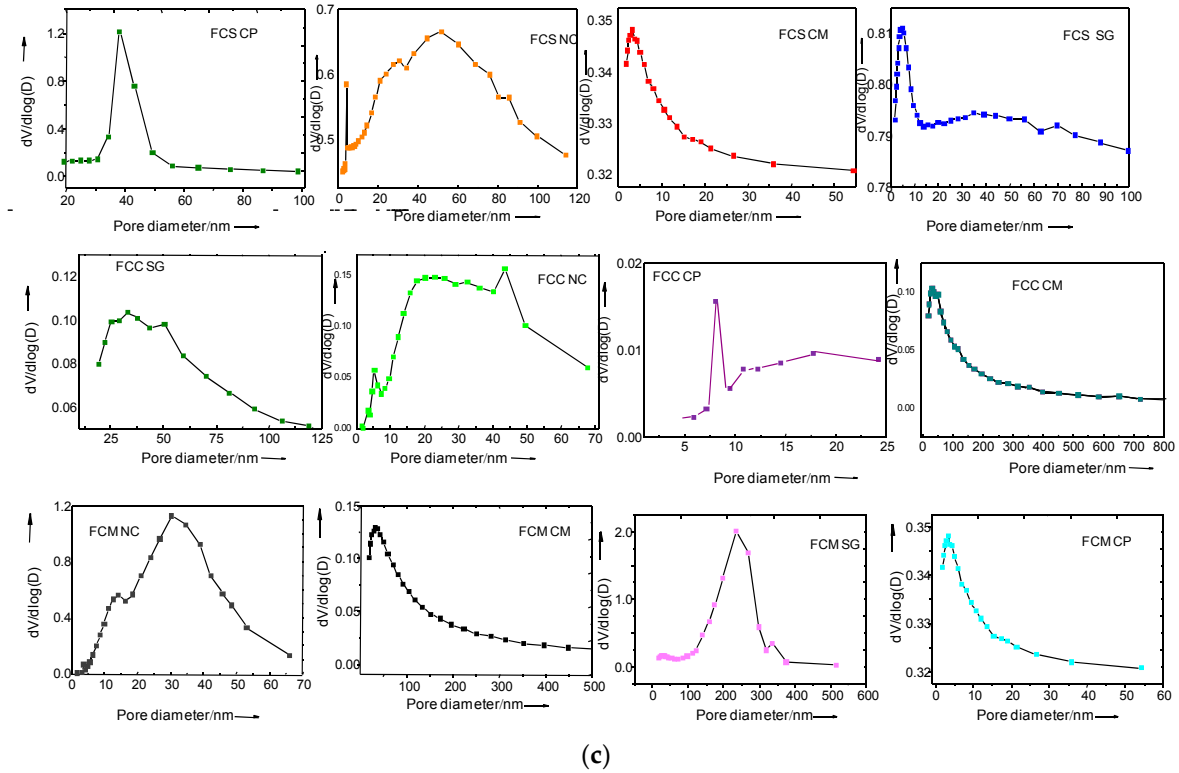

Figure 2. (**a**) The elemental analysis mapping of selected solids: FCS CM, FCC CP, FCC SG and FCM NC. (**b**) Nitrogen physisorption isotherms of the FCS, FCC, and FCM series, and (**c**) pore size distribution curves of the samples.

The spots in the elemental mapping images further reveal the existence of a highly homogeneous distribution of Fe, Co, and Sn at the atomic level on solid surfaces in the FCS series. In contrast, the FCM and FCC have minor concentrations of the third metals on the solid surface. Such an observation could probably originate from the excessive Mo or Cu atomic diffusion during the calcination process at relatively high temperatures, as the Mo or Cu is finely dispersed in certain regions of the solid. Another possibility is that the Mo and Cu precursors pass through a liquid phase before calcination. Thereby, part of the Mo and Cu particles formed could be leached, and this may be the main reason for the resulting lesser amount of the metals on surface.

Table 1 summarizes the textural properties of the solids. The specific surface area of the FCS series varies from 3 to 45 m^2 g^{-1} with the same trends seen for pore volumes in the 0.01–0.18 cm^3 g^{-1} range. Either large crystal formations or metal oxides on solid surface can cause substantial declines in surface area and pore volume, as observed in the SEM images of the FCS CP sample (Figure 1a). Besides, the t-plot micropore areas values are negligible, and the FCS samples are mostly mesoporous, with FCS CP having an opposite behavior. Accordingly, the pore size distributions are typical of mesoporous materials with cylindrical/spherical pore geometry with peaks around 6–15 nm, as found elsewhere [5]. Furthermore, all samples prepared via FCS CP exhibit a BET surface area below 3 m^2 g^{-1}, a pore volume of 0.01 cm^3 g^{-1}, and a pore diameter of ca. 1 nm. This could be recognized as calcination improving the crystallinity of the material, but at the expense of the textural parameters.

The textural parameters of the FCC series are the lowest, when compared with FCS and FCM ones. For instance, FCC CP has a small surface area due to the relatively large crystallite size and the agglomeration of the particles. The average pore size distribution of FCC samples calculated with the BJH method (Figure 2c) suggests that samples have distribution around 0.7–24 nm. The high values of the pore sizes might be because the well developed mesopores through the most domain of crystal structures. These results are well consistent with the t-plot surface areas indicating that

these samples have no micropores. On the contrary, the sample prepared via FCC CP had the worse pore size distributions, as predicted in light of the large crystals shown in the SEM and TEM images. Besides, a significant increase in BET surface area and a greater average pore size could be observed when the sample was prepared via FCC NC.

It was noted that the maximum values of the BET surface area and pore volumes were observed for FCM NC. This is closely related to their poor crystallinity as a result of their nanostructured material, in line with the properties revealed by SEM and TEM. Obviously, the wide pore size distribution curve of FCM NC (Figure 2c) suggests the presence of mesopores with an average pore size centralizing at 18.7 nm (Table 1). Additionally, it is interesting to note that the forming process of a nanosized material may be the main reason for its resulting high textural parameters, as in the case of the FCM SG sample. Both FCM CP and FCM CM have low textural parameters due to the leaching of Co species, causing a somewhat partial collapse of their texture.

2.2. Structure by XRD and Raman

The structural order of samples synthesized is determined with XRD and Raman spectra.

XRD patterns of the synthesized solids are shown in Figure 3. The FCS-synthesized series have patterns characteristic of semi-crystalline solids (Figure 3a), except for those prepared via CM. Indeed, the FCS CM has a crystalline structure, in accordance with SEM and TEM results. However, the interesting phenomenon is that no diffraction peaks appear for the solids synthesized via the nanocasting (NC) route, being amorphous in nature. This is an indication that the dispersion of the species on the surface or pores is favored [20,23]. Thus, detailed inspection on the magnified peaks suggests that some oxide reflections emerged (shown in the figure included at the right side of Figure 3). Otherwise, the species may be below the XRD detection limit. Based on the reflections at about 26.7° (220), 33.0° (220), 35.7° (311), 45.5° (440), 59.4° (511), and 65.0° (440), all patterns have the features of maghemite, namely, γ-Fe_2O_3 (JCPDS-39-1346).

As maghemite arises simultaneously with peaks of magnetite (Fe_3O_4), it is difficult to distinguish them, since their peaks are at the same positions [4]. Additionally, typical diffraction peaks characteristic of hematite as α-Fe_2O_3 appear at 21.2° (012), 38.5° (110), 40.4° (013), and 51.7° (024), especially for FCS CP, FCS CM, and FCS SG. Figure 3a also indicates that the samples synthesized with tin have the expected peaks of the tetragonal rutile structure of SnO_2 at 25.3° (110), 34.0° (101), 38.7° (200), 51.6° (211), and 53.5° (220) with JCPDS card n°. 41-1445. Besides, it is very interesting that in the diffractograms, there is an indication of the formation of Heusler alloys, which matches well with literature reports [24,25]. These types of alloys have a CsCl-type structure and result from the process related to the thermal antisite defects in Fe and Co vacancies, especially for FeCoSn- and FeCoCu-based materials [25]. Moreover, the absence of Co_3O_4 phase in all solids indicates that this phase experiences leaching during synthesis or that Co particles can be finely dispersed in a nanosized manner as a FeCo matrix. This will be further confirmed via Raman and EPR measurements.

It is also noted that the XRD patterns of the FCC series revel few diffraction peaks due to the low crystallinity of the samples, as depicted in Figure 3b. The peaks appearing at $2\theta = 33.2°$ (110), 35.7° (002), and 39° (111) reflections are assigned to be from the monoclinic CuO structure (JCPDS 48-1548). Based on XRD patterns of the FCM series (Figure 3c), all samples show no diffraction lines. This means that the remaining Mo species are well dispersed in the FeCo matrix, as suggested by EDS analyses. Importantly, FCM SG shows a peak at $2\theta = 25.4°$, which can be indexed to the (040) plane from the orthorhombic α-MoO_3 (JCPDS 05-0508) phase. Accordingly, the MoO_3 structure is comprised of corner-sharing chains of MoO_6 octahedra, in which one oxygen atom is unshared, two oxygen atoms are in common with two octahedra, and three oxygen atoms are in part-shared edges and in common with three octahedra [26].

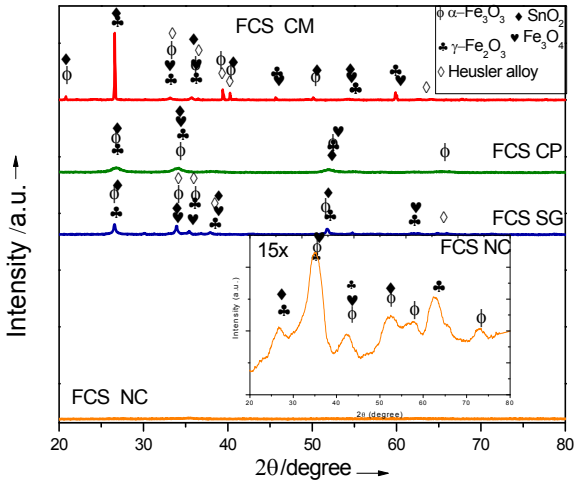

(**a**)

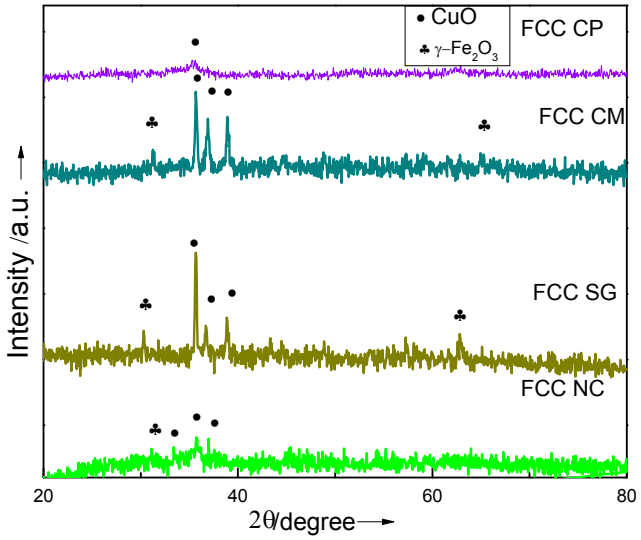

(**b**)

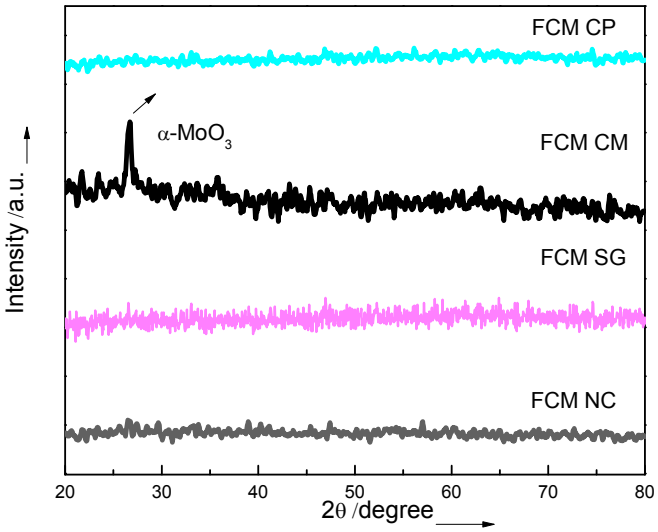

(**c**)

Figure 3. XRD patterns of the synthesized solids: (**a**) FCS series; (**b**) FCC series; (**c**) FCM series.

Thus, through calcination of the samples or hydrothermal ageing at low temperatures, the synthesized solids are semi-crystalline. In some cases, the high temperature of calcination may also cause the segregation of CuO and MoO_3 species as isolated and finely dispersed phases on an FeCo matrix. Notably, this result demonstrates that the addition of Cu and Mo does not markedly change the degree of crystallinity of the samples with the aforesaid Fe phases being formed.

Concerning the preparation method, the decomposition of ferrocene, cobalt, and tin salts in the presence of hydrocarbons and solvents involve the formation of a violet paste via CM. There is a formation of labile oxidized hydrocarbons during this step; thus, it may convert the salts to their corresponding FCS isolated phases, as relatively aggregations of metal oxides particles (SEM results) and/or an alloy was observed, when thermally treated at 700 °C. Furthermore, the alkali precursor used during the sol–gel route plays an important role for the confinement of Fe, Co, and Me (Me = Sn, Mo, or Cu) species inside the FeCo nuclei matrix. Hence, the formation of nanosized crystals of Fe-based species from ferrocene decomposition is likely, as observed in previous work [19,27]. It is worth noting that the cooperative assembly among the co-polymer, the salts, and solvents form a reddish brown solution. In other words, the CP method gives a successful route to have a high dispersion of the phases, after the thermal transformation of the salts. Moreover, it is well-known that the use of a hard template is an efficient method of controlling the crystal growth and morphologies of the solids via NC [20,28]. Besides, the SEM characterization results reveal that that the features of the original mold is preserved, and the final solids have high textural parameters in some cases, even when the materials are calcined at 700 °C.

In agreement, the particle sizes mainly depend on the synthesis method. It is clearly seen in Figure 3 that the particle sizes of the NC method cannot be determined due to the absence of XRD reflections. Meanwhile, the broad peaks of the XRD patterns from CP and SG methods evidence the low-crystalline samples. Contrarily, the particle sizes of some solids prepared via the CM route are determined from the diffraction peak at $2\theta = 42°$ (400) for γ-Fe_2O_3 using the Scherrer equation [20]. As for FCS CM, the nanoparticles agglomerate together and form larger particles of ca. 27 nm due to the crystal growth mechanism, while the particle sizes on FCC CM are 12 nm because of the formation of some nanoparticles. In the case of FCM CM, the nanosized particles are well dispersed in a FeCo matrix and/or their sizes are below XRD limit of detection.

The formation of the phases is confirmed by Raman measurements. In the case of FCS series (Figure 4a$_1$), the Raman features observed at low frequencies correspond to the A_g (221 and 490 cm^{-1}) and E_g (294, 414, 617 and 658 cm^{-1}) vibrations, which are well consistent with the modes of Fe–O vibrations in α-Fe_2O_3,as in the case of FCS NC. Importantly, the mode at 221 cm^{-1} is due to A_{1g} fonon whereas those at 294 and 414 cm^{-1} are associated with the E_g fonon modes, all of them belonging to Fe–O stretching from rhombohedral α-Fe_2O_3 (space group *R-3c* (D^6_{3d})) [4,20]. These modes appear close to that of Fe(III) in distorted tetrahedral symmetry at 294, 473, and 673 cm^{-1}, evidencing that the Fe(III)/Fe(II) ion in octahedral symmetry from maghemite γ-Fe_2O_3 (space group $P4_32$4) exists concomitantly with hematite [8]. This is supported by the broad feature of the FCS NC spectrum and agrees with the XRD observations.

In addition, the Raman features of FCS CM are similar to those of FCS SG, with the modes at 185, 215, 291, 397, 463, 609, and 683 cm^{-1}, being identified as characteristic of maghemite.

Noteworthy, the pronounced modes in FCS CM downshifts to lower frequencies compared to FCS SG, indicating a hardening of the Fe-O, Co-O, or Sn-O bonds due to the higher crystallinity of the former sample, as depicted by XRD. No obvious Raman features of the Fe oxides were observed for FCS CP at low frequency, except for the presence of the modes at 623 and 665 cm^{-1}, identified as being from both hematite and maghemite.

The literature reports that the Raman spectra of γ-Fe_2O_3 and Fe_3O_4 have similar features and phonon modes are indeed very close [12]. Therefore, these oxides may appear concomitantly, as seen in XRD spectra. Additionally, Raman vibration modes at 476 cm^{-1} is associated with the E_g mode due to oxygen atoms in the oxygen plan vibration, whereas those at 632 and 687 cm^{-1} are ascribed to A_{1g}

and B_{2g} vibration modes, since those vibration modes are induced by the expansion and contraction of the Sn-O bonds in tetragonal rutile. This finding is in very good agreement with the optical active Raman characteristic of the SnO_2 structure (space group P4/mnm (D_{4h}^{14})) [29], in addition to those of Fe-related phases.

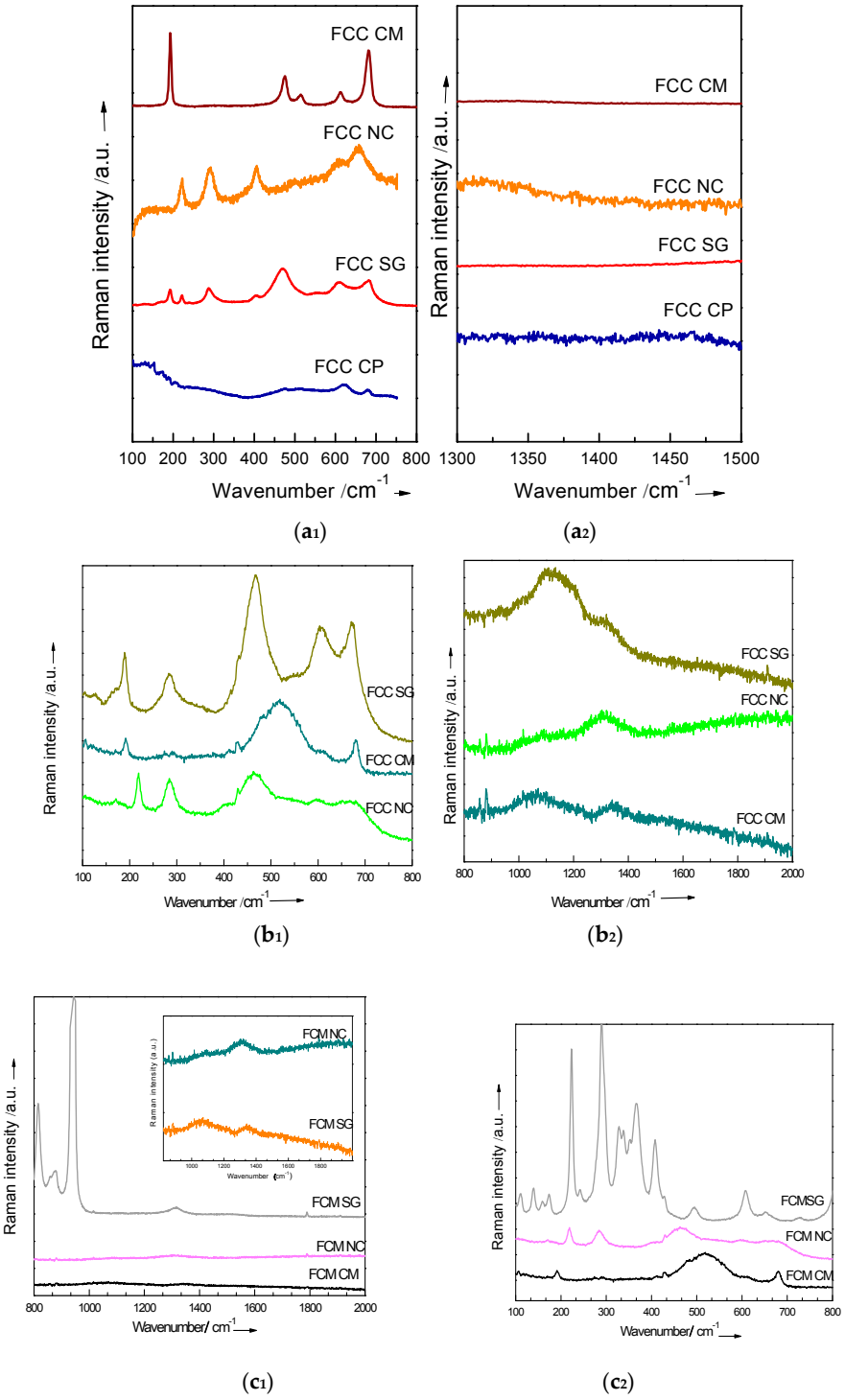

Figure 4. Raman spectra of the solids synthesized: (**a**) FCS series; (**b**) FCC series; (**c**) FCM series. The number *1* indicates the spectra taken at low frequencies, whereas the number *2* indicates the spectra taken at high frequencies.

At the higher frequency region (Figure 4a_2), all bands are broad and the vibrations in the 1159–1345 cm^{-1} range for FSC NC and FCS CM can be attributed to the hematite phase [19]. Small vibrations on these sample at 1092, 1227, and 1264 cm^{-1} suggest the presence of either hydrocarbon debris from the synthesis or oxygen defect vacancies [19]. Additionally, the bands at 1316 and 1603 cm^{-1}, respectively assigned to be from D and G bands due to the presence of hydrocarbon residues, cannot be ruled out, as observed previously [8]. On the contrary, a broad Raman band at 1313 cm^{-1} is attributed to the A_{1g} and E_g modes of maghemite, as seen in the spectra of FCS SG and FCS CP.

One should note that the presence of segregated SnO_2,phases or phases containing Fe, e.g., Heusler alloys, is routinely encountered in studies of ternary FeCoMe systems (where Me indicates other metals) [25]. This is also explained by the relatively high temperature of ca. 700 °C as promoting the formation of the segregated phases and seems to confirm the observations of XRD, which exhibits samples of nanosized feature with low crystallinity.

Although the Raman spectra of the FCC series (Figure 4b_1) have broader bands than those of the FCS series, the modes of the former are found in similar positions and frequencies of those of hematite and maghemite. Moreover, modes at 284 (Ag), 333 (Ag), and 622 (Ag) cm^{-1} are comparable to the Raman active optical phonons of monoclinic CuO (C^6_{2h} space group), in good agreement with the previously reported data [30]. These modes may be superimposed to those of hematite and maghemite, evidencing that Cu addition has an impact on decreasing the crystallinity of the samples. Moreover, the expected CuO modes appearing at 282, 333, and 622 cm^{-1} may be in the same position as those of Fe-related phases due to the broadness of the spectra. At high frequencies, the Raman spectra confirm the presence of hematite and magnetite through the bands at 1120 and 1343 cm^{-1} (Figure 4b_2). Due to the strong luminescence during the measurements, the FCC CP spectrum is not obtained. In addition, the low crystalline nature of the FCC series is reflected by the wideness of the Raman bands, in good agreement with the previously XRD reported data.

On the contrary, the FCM series (Figure 4c_1) displayed Raman spectra with no dissimilarities with those of the FCS and FCC series, with FCS SG being an exception. This fact reveals the dependence only of the synthesis method on the hematite and maghemite presence. These findings are not interpreted as the addition of the third metal determining neither significant change in the nanocrystalline features of the solids nor the phases formed. Besides, FCM SG gives a mode at low frequencies ranging from 111 to 728 cm^{-1}, which is related to the typical Raman modes of orthorhombic α-MoO_3 ($D_{2h}{}^{16}$ *Pbnm* space group). Besides, the modes located at 275, 330, and 369 cm^{-1} are associated with the O–Mo–O scissoring and the O=Mo=O wagging modes, respectively [26,31]. The vibrations along with that at 657 cm^{-1} are assigned to the triply coordinated oxygen (Mo3-O) stretching mode, which results from edge-shared oxygen in common with three octahedra [31]. Such modes may be positioned in the same regions as those of the Fe-related phases identified in the nanomaterials under study.

At high frequencies (Figure 4c_2), the expected modes of hematite and maghemite are visible through the modes at 1162 and 1320 cm^{-1} or only one of them. Specifically for FCM SG, the strong band at 943 cm^{-1} is due to the symmetric stretching of the short Mo–O terminal bonds along with a weak and medium band at around 878 and 812 cm^{-1}, both assigned to be from the vibrations of the Mo–O–Mo bridge [31].

According to the findings, the modes attributed to being from Co_3O_4 arise at 482 (E_g), 519 (A_{1g}), and 621 and 690 cm^{-1} (F_{2g}) [12]. Thus, the absence of Co-related phase modes in all spectra indicates that cobalt would coexist with Fe-related phases, but the intensity of the latter species is too weak to be measured.

In short, a series of FeCo-based catalysts were prepared via four main routes. The calcination of the solids in air results in the burn of part of the carbon during the carbonization process, so carbon serves as the reducing agent of the Fe and Co to form maghemite, magnetite, and CO_2. However, this does not prevent the Fe from oxidizing by air, thus preserving the hematite form. This observation is consistent with the formation of the aforesaid phases, independently of the preparation method,

as observed via XRD and Raman spectra. On the contrary, the morphology and textural parameters are dependent on the preparation method, according to SEM-EDS, TEM, and textural parameters results.

2.3. EPR Measurements

EPR measurements were taken to gain further insight into the composition of the selected samples, especially for the location and state of Fe and Co (Figure 5). The EPR spectra recorded for FCS SG and FCM CM show one broad resonance signal with line widths of 3.0 and 3.8 kG (Figure 5). In all of these cases, the electron-free energy values, i.e., g is equal to 2.1. According to the findings, the signal at g = 2.0 can be ascribed to the very likely octahedral coordination or extra-framework form of iron species [17,32]. Thus, the observed shift of 0.1 for the g value can be attributed to the agglomeration of the nanoparticles, resulting in strong dipolar interactions, as for FeCo magnetic compounds [32]. Evidence for the nature of iron as Fe^{2+}/Fe^{3+} has been recently reported in our previous findings on detailed EPR studies of Fe-based compounds [17], and this confirms the maghemite presence, as previously observed via Raman and XRD.

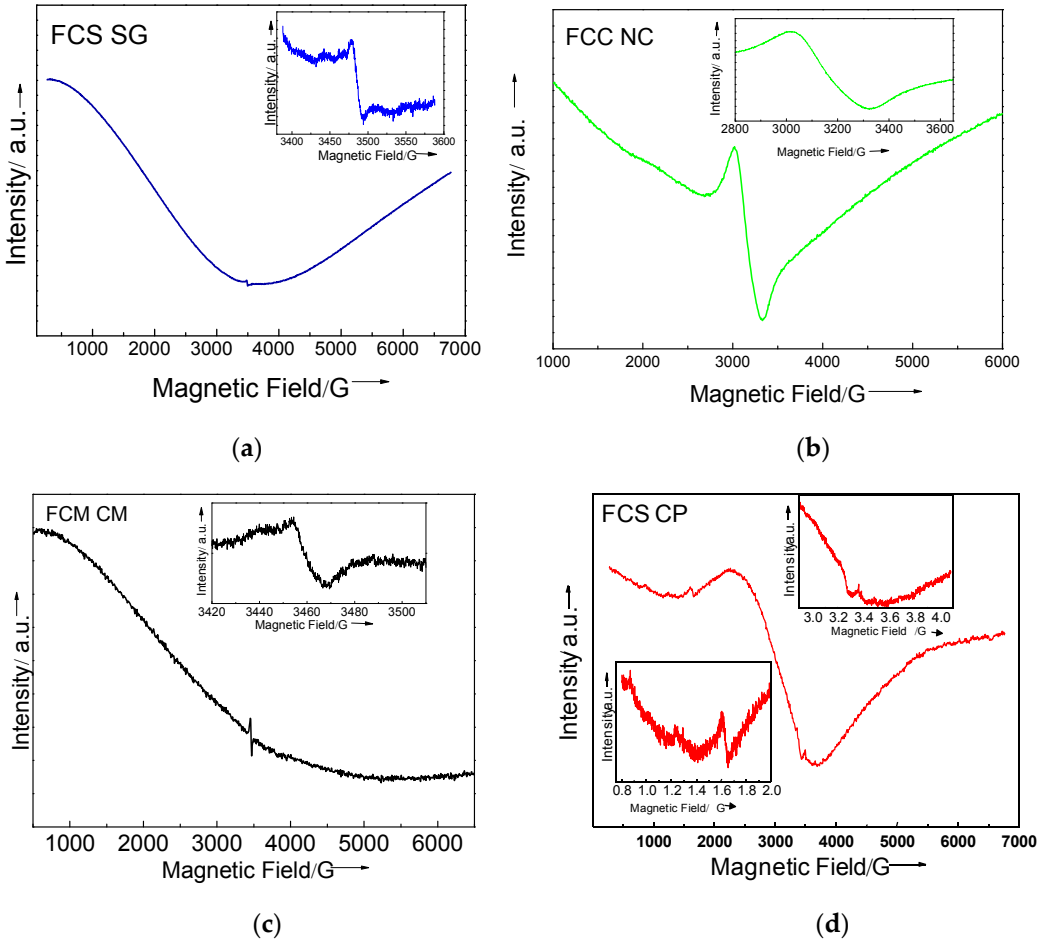

Figure 5. EPR spectra of selected solids: (**a**) FCS SG, (**b**) FCC NC, (**c**) FCM CM, and (**d**) FSC CP. The included figures show a specific region of the spectra.

In addition, the tetrahedral coordination of iron with strong rhombic distortion or framework form appears at g = 4.3, well corresponding with Fe(III) presence in the structure [17]. Furthermore, the findings assign the g value close to 4.3 to the super exchange between Fe^{3+}, Co^{2+}, and Co^{2+}/Co^{3+} [17,32–34]. This can be inferred in light of the signals in Figure 5 below the main line. Therefore, the presence of these species in all solids cannot be ruled out. FCS CP and FCS

NC have spectra with signals of Fe in two regions. All of these contributions gave the conclusion that the resulting solid is composed predominantly of the following species: Fe^{3+}/Fe^{2+} (γ-Fe_2O_3), Fe^{3+} (α-Fe_2O_3), and Co^{2+}/Co^{3+} (Co_3O_4), the latter being finely dispersed as an FeCo matrix.

Besides the signal in g = 2.1, a broad ferromagnetic resonance line may overlap the signal of Sn^{4+} (SnO_2 phase), Cu^{2+} (CuO), and Mo^{6+} (α-MoO_3) with a hyperfine structure at a g value of around 1.9–2.1 (magnetic field 3.0–3.8 kG) [34–36], as demonstrated by the curve in Figure 5 above the main line. Because these signals are relative complex, it is hard to assign them to a definite a proper oxidation state.

From the EPR obtained results, it is clear that the samples have the same nature in terms of oxidation states, with the formation Fe^{2+}/Fe^{3+} Fe^{3+} and Co^{2+}/Co^{3+} predominantly on the surface as an FeCo matrix and Sn^{4+}, Cu^{2+}, or Mo^{6+}, depending on the third metal present on the solid. These results are in full agreement with those of the XRD, Raman, and EDS studies.

To sum up the characterization results, it can be inferred that the techniques for synthesizing FeCo-based catalysts used in this work comprises nanocasting (NC), sol–gel (SG), co-polymer assisted co-precipitation (CP), and chemical modification (CM). A comparison between unique features of the preparation methods shows that CM has the advantage of being an easy route to obtain stable materials in relatively large amounts, in spite of their low textural properties and difficulty in achieving nanosized structures, as observed via SEM-EDS, TEM, XRD, Raman, and textural properties.

On the contrary, the most widely method for preparing solids is the sol–gel followed by the hydrothermal method [6,8]. This route involves one-pot hydrothermal process, through the processing of metal salt or metal alkoxide precursors, which is not time consuming for the practical applications. Besides, it displays the characteristics of requiring conditions of short or long aging time. Indeed, as low heating produces solids with a semi-crystalline structure and nanosized features at relatively low reaction temperature during synthesis trials, in line with the characterization results.

CP is an extremely versatile route since it allows for the formation of a large variety of metal oxides at relatively low temperatures. Though this method, nanosized features can be attained in the prepared materials by adjusting the synthesis conditions using a soft template, e.g., co-polymer [37]. However, the main challenge of obtaining nanosized materials via CP is the sintering of the particles forming solids with low textural parameters, as observed in this work.

The preparation of solids via NC consists in using a hard template to obtain materials with regular and controlled morphologies by adjusting the morphology of the applied template, after removal of the latter by selective chemical etching or thermal decomposition in a multi-step procedure [20]. Hence, the formation of materials with nanoporous solids with a semi-crystalline structure and large pore sizes were observed. Additionally, some samples have their morphology destroyed during post-removal of the template, and these materials are not the inverse replica of the original template.

2.4. Activity Tests for Styrene Oxidation

The catalytic performance of all solids was investigated in the styrene oxidation with H_2O_2 as an oxidant and acetone as a solvent (Figure 6).

It can be seen from the data in Figure 6 that all catalysts were active in the reaction, under the same conditions studied. This demonstrates that the γ-Fe_2O_3 and α-Fe_2O_3 monoxides present on the solids promote the oxidation of styrene, as reported in the literature [17,38,39]. Indeed, our previous results have shown that the styrene conversions of α-Fe_2O_3 and Co_3O_4 monoxides are 3.0% and 6.8%, respectively [17], which is considered to be too low for the solids. On the contrary, the nanosized cobalt phase in FeCo likely contributes to the activity of the whole set of samples. Additionally, the results provide evidence of extensive promotion of cobalt already at the beginning reaction, resulting from its intrinsically higher oxidation ability than Fe. Hence, the catalytic activity of the solids was assessed in the styrene oxidation due to the combination of Fe and Co.

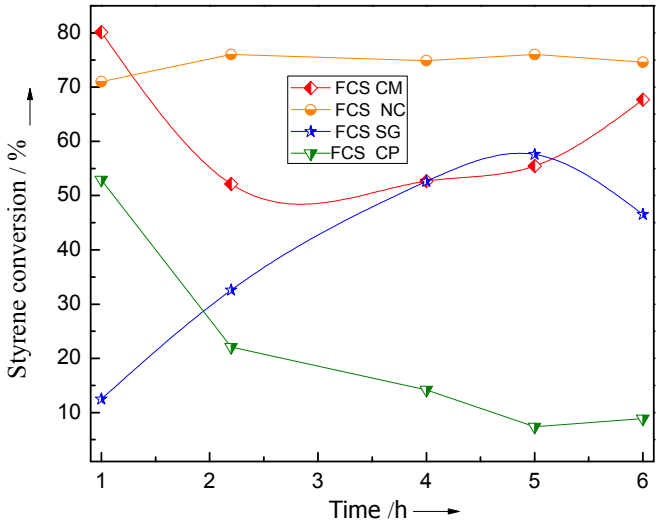

(**a**)

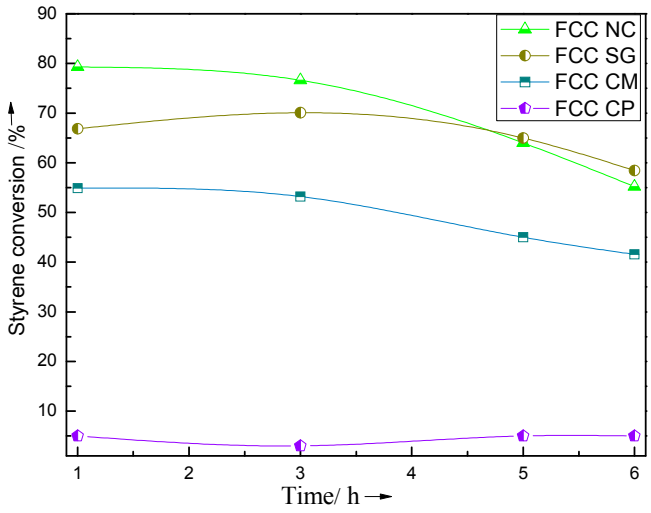

(**b**)

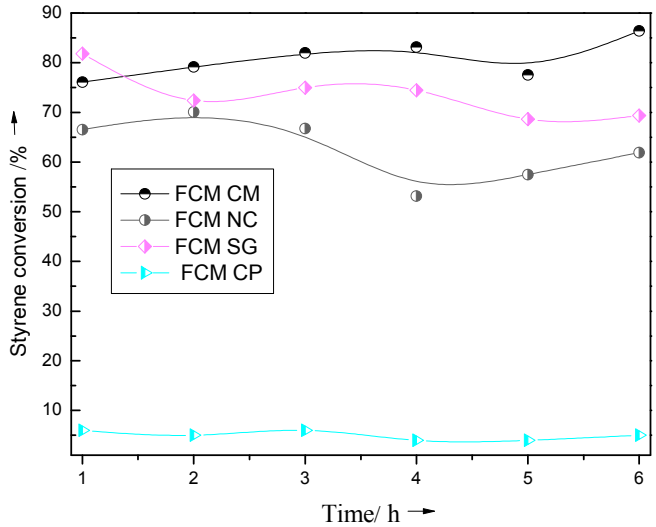

(**c**)

Figure 6. Styrene conversion in function of the reaction time: (**a**) FCS, (**b**) FCC and (**c**) FCM. Reaction conditions: a temperature of 50 °C, styrene-to-H_2O_2 molar ratio of 1 in the presence of acetone and 0.1 g of catalyst.

The reaction conditions in liquid phase oxidation reactions have long been known to markedly affect the composition, textural properties, and crystallinity of the solids, altering the activities of the Fe-containing catalysts in the styrene oxidation ([12] and references herewith). Therefore, these changes do not seem to play a role in the styrene oxidation reaction, when using mild reaction conditions. Indeed, reactions conducted without catalysts have a 3% conversion. Additionally, previous studies have shown that a FeCo catalyst itself has only a 17.8% styrene conversion [17], clearly implying that the preparation method and the addition of the third metal to FeCo contribute to a better catalytic performance.

At the beginning of the reaction, the catalysts converted far more than 5% styrene, independently of the preparation method used to obtain the solids. Prolonging reaction time, however, a distinct behavior was observed due to the stability of each solid in the reaction media.

The styrene conversion declined quickly with FCS CP and FCS CM solids, whereas FCS SG experienced an opposite trend, and conversion over FCS NC was steady (Figure 6a). After 3 h of reaction, styrene consumption increased on FCS CM, following the same trend as that of FCS SG. At this stage, the high porosity of FCS SG seemed to be able to offset the deactivation of the solid. Furthermore, it is interesting that XRD and Raman data show that, despite the high crystallinity, the FSC CM is very active at the end of the reaction. This is most likely due to the synergistic effects of the dispersion Sn^{4+} sites' and porosity of the solid (textural properties, EPR and SEM-EDS results), which in turn served to facilitate the exposition of the reactants to the active sites and induce enhanced catalytic performance.

Interestingly, FCS NC was the most active catalyst among the FCS series of solids studied, reaching more than 70% with an unchanged result along of 6 h. Besides the existence of the synergetic effect between FeCo matrix and Sn species, the FCS NC had the additional advantage of being produced via nanocasting. The latter method implies that Sn acted as a promoter on the surface of the nanocasted matrix, with a positive effect in this oxidation reaction.

In the case of the FCC series (Figure 6b), the conversion of styrene decreases as the reaction time increases. The solids reach a conversion of more than 55% at first, and this conversion then slightly drops by 8% at the end of the reaction. On the other hand, the conversion of FCC CP remains below 5% because of a reduced surface area and pore volume. Additionally, a large surface area affords numerous reaction sites, and a low crystallinity favors the catalytic activity of FCC NC and FCC SG, achieving 60% styrene conversion in 6 h of reaction. Hence, the physicochemical features of FCC catalysts for styrene oxidation are dependent on their morphology, phases, and crystal size. The fast adsorption of the reactants towards the nanoparticles produced via SG as well as the diffusion of the reactants to the nanostructure obtained via NC make the FCC NC and FCC SG responsive to surface redox reactions, while reducing the probability of their deactivation.

With respect to the third metal influence, the CuO presence does not allow for increased conversions, compared with SnO_2 in the FCS series. The nanocrystalline samples possessing Fe, Co, and Sn in high oxidation states can effectively increase the redox ability of the catalysts, as compared to the combination of Fe, Co, and Cu in FCC catalysts. A comparison between the FCS and FCM series demonstrates that the Mo addition in the α-MoO_3 form increases the styrene conversion, at the same level as that of FCS materials. Other findings have shown that the addition of metals to Fe-based materials is also helpful in improving the structural, textural, and electronic properties of the solids for a desired application [40–44].

Figure 6c illustrates the performances of the FCM series. The conversion of styrene reaches values superior to 60%, with FCM NC, FCM SG, and FCM CM achieving the best performances. Nevertheless, styrene conversion is nearly 5% with FCM CP, well consistent with the FCS and FCC series. It seems that an appropriate combination of low textural properties and surface exposition of the promoters is unfavorable to the reaction, which is indeed the main feature of the solids prepared via CP. Through results, it is also shown that SG and NC methods produce porous materials with nanocrystalline phases and geometric structures that is another important aspect related to catalytic

performance. In addition, the FCM CM catalyst performs better than FCM NC and FCM SG catalysts because the α-MoO_3 species forming reoxidation couples among Fe and Co or among Co and Mo enhance the styrene conversion.

Table 2 summarizes the conversion of styrene, hydrogen peroxide efficiency, and the selectivity of the products obtained in 6 h of reaction.

The FCS NC, FCS CM, FCC NC, FCC SG, and FCM CM catalysts exhibit the highest conversions (>55%), confirming that the NC route produces a porous inverse replica of the template helping to attain disordered structures undoubtedly bring about a high activity in the epoxidation of styrene. In the case of CM, Sn and Co introduction in FeCo may suppress the deactivation of Fe^{3+} through the immediate proximity of the metal promoters in the lattice of a given catalytically active Fe phase that enhances the conversion. For FCC SG, the combination of SG nanosized features and Cu addition produces a good performance in the reaction.

Table 2. Catalytic performance of the solids in the oxidation of styrene using hydrogen peroxide as an oxidant. Reaction condition: Styrene-to-H_2O_2 molar ratio of 1, a 100 mg of catalyst, a temperature of 50 °C, and 6 h of reaction. The compounds benzaldehyde (Benz), acetophenone (Acet), ethylbenzene (EB), 2-fenyl ethanol (PEt), 2-fenyl acetic acid (PAc), and 2-fenyl acetaldehyde (PAcet) are the major products obtained. Others include products of styrene polymerization.

Sample		Conversion (%)	Efficiency of H_2O_2 (%)	Selectivity (%)						
				Benz	Acet	EB	PEt	PAc	PAcet	Others
FCS	NC	74.6	24.3	27.7	5.4	13.3	21.5	29.3	2.8	-
	SG	46.5	21.8	23.8	4.2	14.5	31.9	24.2	1.4	-
	CM	67.7	16.9	25.4	3.1	11.7	26.5	33.3	0.9	-
	CP	8.9	2.4	9.6	-	28.8	11.5	-	0.1	50.6
FCC	NC	55.2	13.7	12.0	5.9	10.6	30.7	29.2	1.5	10.1
	SG	58.4	12.1	13.7	1.5	15.1	26.6	26.2	0.4	16.5
FCM	CM	41.2	9.3	14.2	8.5	15.3	27.3	25.9	4.0	15.8
	CP	5.0	1.6	9.6	-	24.5	9.9	-	-	56.4
	NC	69.3	23.0	15.4	7.0	12.7	24.1	25.6	0.5	14.2
	SG	62.0	20.5	16.6	5.5	13.2	20.8	22.9	0.2	12.5
	CM	86.2	21.7	17.0	5.0	15.5	22.4	25.6	0.3	13.8
	CP	4.8	1.8	12.9	-	23.8	10.6	-	-	52.7

Therefore, the inferences that can be drawn from the conversion results are that nanosized catalysts prepared via NC and CM are highly active in the oxidation of styrene with H_2O_2 oxidants. This may be due to the fact that their high textural properties expose more active sites to the reactants during the catalytic reaction. Additionally, the high dispersity of Mo^{6+}, Cu^{2+}, and Sn^{4+} species on the FeCo matrix is found to be most effective for styrene oxidation. Studies on Fe-based materials for adsorption and photocatalytic applications have shown that the performances of the solids can be associated with the particle sizes and dispersion of the solids, in agreement with our work [45,46].

Concerning the influence of the third metal addition, a direct correlation between the valences of the promoters and the catalytic activity can be established, as follows: $Mo^{6+} > Sn^{4+} > Cu^{2+}$. This preferential enhancement may be due to the variable valences of iron and cobalt in the FeCo, which favors the cleavage of the double bond in styrene on the Fe^{3+}/Fe^{2+} and Co^{3+}/Co^{2+} surfaces. Since the SnO_2, α-MoO_3, and CuO monoxides have styrene conversions inferior to 10% in 6 h of reaction [17], the hexavalent and tetravalent oxidation states of Mo^{6+} and Sn^{4+} ions favors the adsorption of H_2O_2 and styrene together with the help of the FeCo matrix, thereby contributing to enhanced catalytic activity.

Usually the hydrogen peroxide efficiency has a great influence on catalytic performance due to the coordination of H_2O_2 on the active Me^{3+} metal sites as an initiation step of the styrene oxidation reaction [12,38]. Hence, all solids show an H_2O_2 efficiency superior to 10%, which means that H_2O_2 acts as an oxidant to promote styrene oxidation products. The lowest values of H_2O_2 efficiencies

are achieved over solids prepared via CP methods (Table 2) because of their low exposed surfaces, as demonstrated in Table 1. Another factor to consider is that the surfaces of Sn- and Mo-containing catalysts are capable of decomposing H_2O_2, which is likely attributed to their high valences compared to those of Cu. Surface species such as Fe^{2+}/Fe^{3+} (γ-Fe_2O_3), Fe^{3+} (α-Fe_2O_3), Co^{2+}/Co^{3+} (Co_3O_4), Mo^{6+} (α-MoO_6), and Sn^{4+} (SnO_2) probably plays an important role in binding to H_2O_2, thus catalyzing the reaction, as suggested by XRD, Raman, and EPR results. As can be seen in Table 2, benzaldehyde, 2-phenyl ethanol, 2-phenyl acetic acid, and ethylbenzene are the major products obtained with 2-phenyl acetaldehyde and acetophenone produced in lesser amounts for the FCS series. These products are valuable chemical intermediates used in perfumery and exhibit fungi bacteriostatic activities [39,47]. On the basis of the styrene oxidation mechanism, styrene oxide and benzaldehyde are the expected products [48,49], even though the former is not produced. This means that the main products benzaldehyde and styrene oxide are formed, but styrene oxide further reacts, yielding 2-phenyl ethanol, 2-phenyl acetic acid, and 2-phenyl acetaldehyde. In addition, styrene C–C bond cleavage preferentially gives benzaldehyde and ethylbenzene, as an elimination reaction product [50]. In fact, these products are generated by a secondary and consecutive reaction between benzaldehyde and styrene epoxide [17], as summarized by the reaction paths illustrated in Reaction II.

When FCS NC was used as a catalyst, a 74.6% conversion with 27.7% selectivity of benzaldehyde and 50.1% of the sum to 2-phenyl ethanol and 2-phenyl acetic acid was observed. Similarly, the others samples of FCS series followed the trend of the selectivities, except for FCS CM. The latter sample had 50.6% of the sum of the polymerization of styrene products, which tended to be observed in the other CM samples as well. Although lower conversions were exhibited in CP samples, there was a very high selectivity for the polymerization of styrene products at the expense of the other products. Thus, it suggests that the preparation method as well as the nature of the third metal addition have a greater effect than the oxidation state of the Fe center, in contrast to our previous reports [12].

By adding Cu as the third metal to FeCo, i.e., FCC series, benzaldehyde, acetophenone, ethylbenzene, 2-phenyl ethanol, phenyl acetic acid, 2-phenyl acetaldehyde and styrene polymerization products were detected, and this was independent of the preparation method used. Among them, 2-phenyl ethanol and 2-phenyl acetic acid formation were significantly high (>50%) as a result of the styrene epoxide side reactions. Low-valence complexes bearing Cu(II) ligands have been reported to be highly catalytically active sites for olefin epoxidation, especially for styrene polymerization products [51]. This apparently shows that the Cu in FeCo goes through the formation of oxidation and polymerization of styrene reactions, even though iron itself is a promising transition metal for producing benzaldehyde and styrene epoxide [49,51].

A trend similar to that for FCC was observed for the FCM series with regard to the selectivity of the products, having a maximum value of about 50% for 2-phenyl ethanol and 2-phenyl acetic acid, in addition to styrene polymerization products. Thus, taking into account the participation of Mo as a promoter in the FeCo matrix, the Mo^{6+} species seems to undergo available surface sites, which readily oxidize styrene in a fashion similar to that of Cu^{2+}. In line with these results, Mo complexes have been reported as effective catalysts for producing selectively styrene oxidation products [51].

Though the CM samples show lower selectivities to the main products than their neat NC and SG counterparts, CM selectively provides the formation of styrene polymerization products. The CM procedure has hampered the samples' practicality due to the necessity of multistep syntheses and expensive reactants during synthesis.

Owing to the semi-crystalline structure, porosity and availability of the active sites in the solids, the NC method allows a structure–activity correlation with the valuable oxidation products mechanism. To better explain this phenomenon, the surfaces of the spheres and the walls of the broken spheres possessing dispersed Mo^{6+} or Sn^{4+} species with redox properties can easily convert styrene into the observed compounds, providing valuable products with good selectivity.

3. Experimental Section

3.1. Synthesis of the Solids

A three series of solids, namely, FeCoSn, FeCoMn (FCM), and FeCoCu (FCC) were synthesized using the following methods: copolymer-assisted co-precipitation of iron precursor (CP), chemical modification (CM), sol–gel (SG), and nanocasting (NC).

The copolymer-assisted co-precipitation of metal precursors (CP) method consisted in dispersing 0.36 mmol Pluronic P-123 (Sigma-Aldrich, St. Louis, MO, USA) co-polymer in 60 mL of a 1 wt % hydrochloric acid solution to depolimerize the reactant, under stirring [22]. Then, about 6.5 mmol tin chloride (Isofar) and 6.5 mmol cobalt nitrate (Vetec) solutions were simultaneously added into a flask containing the previous solution. The resulting yellowish brown suspension was added slowly into a beaker containing 30 mL of a 1.0 mol L^{-1} aqueous solution of sodium carbonate, under vigorous stirring. Afterwards, 13 mmol ferrocene (Aldrich) and 19.9 mmol citric acid (Synth) were mixed to the previous suspension at room temperature. The pH of the final solution was adjusted to 7 using an aqueous solution of sodium hydroxide (2 M). After all the reactants were added, the reddish brown suspension formed was stirred for 5 h at room temperature and was then aged under autogenous pressure conditions at 50 °C for 5 days. Subsequently, the precipitate formed was filtered, washed deionized water, and dried at 30 °C overnight to produce a yellow precipitate. The obtained powder was then calcined at 700 °C for 5 h in a static air atmosphere and named as an FCS CP solid. The letters FCS represents the Fe, Co, and Sn metals, whilst CP indicates that the solid was synthesized via copolymer-assisted co-precipitation.

The chemical modification of Fe ions (CM) route was based on previous reports [19], with modifications. Briefly, a 0.12 mol paraminobenzoic acid was dispersed in 15 mL of Triton X-100 (Aldrich) and magnetically stirred for 10 min. Then, 30 mL of furfural was added dropwise into the previous mixture under vigorously stirring to allow the solution to obtain a uniform aspect. Subsequently, the mixture was continually stirred while adding 47.6 mmol citric acid and 13 mmol ferrocene (Aldrich) for 20 min. The following step was the addition of 6.5 mmol tin chloride and 6.5 mmol cobalt nitrate solutions to the mixture under mechanical stirring for another 30 min at room temperature. The obtained solid was dried overnight at room temperature and the violet product was calcined at 700 °C for 6 h to have FCS CM. The letters FCS represents the Fe, Co, and Sn metals, while CM indicates that the solid was synthesized via chemical modification.

The sol–gel (SG) route was applied to obtain the FCS SG solid, based on previous findings, with modifications [8]. Typically, 0.18 mmol polyvinylpyrrolidone (Sigma-Aldrich, St. Louis, MO, USA)) was dissolved in a 50% (v/v)) of isopropyl alcohol under constant stirring for 10 min. Then, 15.6 mmol citric acid and 13 mmol ferrocene were added to the previous solution. After the suspension was stirred for additional 10 min, 6.5 mmol cobalt nitrate (Vetec) and 10 mmol tin chloride (Isofar) aqueous solutions were added drop-by-drop to the mixture, and stirring was continued for 2 h. The reddish brown mixture was introduced into a Teflon-lined stainless steel autoclave at 180 °C for 9 h. Then, the resulting black precipitate was filtered and washed several times with deionized water and subsequently calcined at 700 °C in an air flow. Importantly, the letters FCS represent the Fe, Co, and Sn metals, whereas SG indicates that the solid was synthesized via sol–gel.

Nanocasting (NC) consisted in the use of a hard template such as XAD-16 (Aldrich). In a typical synthesis [20], about 10.0 g of the resin was dispersed in 40 mL of deionized water under stirring for 10 min. This step was repeated several times to give the solution a pH level of 7, and the resin was then dried at 50 °C for 24 h. Simultaneously, solutions containing 13 mmol iron nitrate and 6.5 mmol tin chloride and cobalt nitrate were prepared. About 20 mL of the aforesaid solutions were added to 2 g of XAD-16 resin under stirring for 2 h. Finally, the solid was washed followed by drying at 60 °C overnight and calcination at 700 °C for 8 h, obtaining a solid labeled as FCS NC. The letters FCS represent the Fe, Co, and Sn metals along with CM, indicating the solid was synthesized via chemical modification.

Two other series of solids were synthesized in a similar fashion as described above, changing the third metal for Cu (copper nitrate, Vetec) or Mo (ammonium heptamolybdate precursors, Isofar), and these series were labeled as FCC and FCM, respectively.

Therefore, the general nomenclature adopted in this work consisted of the letters *FCX* followed by the synthesis method, i.e., *CP*, *NC*, *SG*, or *CM*. For instance, in the expression "FCM NC", FCM indicates the Fe, Co, and Mo metals, respectively, and NC indicates that the sample was obtained via nanocasting.

3.2. Characterization of the Catalysts

Powder X-ray diffraction (XRD) patterns were recorded on a Bruker D8 Advanced diffractometer (Bruker, Karlsruhe, Germany) using Cu Kα radiation at 40 kV and 25 mA. The step size was 0.02° and the scan range of 10–80°. The diffraction patterns were compared with those included in the JCPDS (Joint Committee of Powder Diffraction Standards) database.

The specific surface area, the total pore volume, and the average pore diameter were determined via nitrogen physisorption isotherms at −196 °C. The experiments were performed using an ASAP 2420 instrument (Micrometrics, Norcross, GA, USA). The samples (ca. 0.1 g) were thermally pretreated via outgassing in a vacuum at 150 °C for 10 h to remove the adsorbed moisture. Surface areas were calculated with the Brunauer–Emmett–Teller (BET) method, whereas pore size distributions were determined with the Barrett–Joyner–Halenda (BJH) method.

Raman spectroscopy studies were carried out using a triple Jobin-Yvon T64000 spectrometer coupled to charge-coupled device (CCD) detector. The argon ion laser in a power of 0.3 mW was used to obtain the Raman spectra in the 100–4000 cm^{-1} range. The Olympus objective lens with a focus of 100 times was used and the laser line was at 785.8 nm.

Inductively coupled plasma optical emission spectroscopy (ICP-OES) were carried out with a Perkin Elmer spectrometer. Before the analyses, samples were digested in a hydrochloric acid and nitric acid solutions in a sand bath at 200 °C. After solvent evaporation, 1 wt % nitric acid and water were added to the resulting precipitate to determine the metal concentrations.

Scanning electron microscopy (SEM) images and Energy Dispersive X-ray spectroscopy (EDS) analysis were performed on an FEI, Quanta 200 FEG model microscope (FEI, Hillsboro, OR, USA). Samples were prepared via gold sputtering on their surfaces and deposited onto aluminum stubs coated with a carbon film.

Transmission electron microscopy (TEM) was performed using a JEOL JEM 2010F electron microscope (FEI Quanta, Hillsboro, OR, USA) running at 200 kV. Prior to the analyses, the solids were sonicated in ethanol for several seconds and then dried and dropped on the TEM grids. Some images were taken in an FEI Tecnai20 G2 200 kV electron microscope.

Electron paramagnetic resonance, EPR spectra were recorded on a Bruker spectrometer (Bruker, Rheinstetten, Germany) with a high frequency modulation of 100 kHz. The X-band microwave frequencies were close to 9.5 GHz. Before the measurements, the solids were loaded in an EPR quartz tube under a helium atmosphere. All the measurements were carried out at 293 K. The *g* factor values were determined through the simultaneous measurements of the magnetic field magnitude and the microwave frequency [12].

3.3. Catalytic Evaluation

Styrene oxidation was conducted using a batch glass reactor equipped with a thermocouple, a reflux condenser, and a gas inlet at atmospheric pressure. In the oxidation reactions, typically 0.1 g of catalyst, 10 mmol styrene, 10 mmol dilute H_2O_2 (30%), and acetone were introduced into the reactor. Then, the reaction was carried out at 50 °C for 6 h. The reaction mixture was allowed to cool down to room temperature. The products were analyzed via gas chromatography using a GCrom apparatus. The identification of the products was by means of gas chromatography coupled to mass spectrometry (GC-MS) device in a Shimadzu GCMSQP5050 equipment (Shimadzu, Kyoto, Japan). Xylene was used

as internal standard. The performance of the solids was calculated on the basis of styrene conversion, H_2O_2 efficiency, and selectivity of the products [17], as follows:

$$\%\text{Styrene conversion} = \frac{\text{Styrene in} - \text{Styrene out} \times 100}{\text{Styrene in}} \quad (1)$$

The selectivity of the products formed was determined based on the conversion of styrene:

$$\%\text{Selectivity to product i} = \frac{\text{mols of product i produced} \times 100}{\text{mols of reacted styrene}} \quad (2)$$

$$\%\text{Efficiency of the } H_2O_2 = \frac{\text{Amount of } H_2O_2 \text{ used for oxidation} \times 100}{\text{Amount of } H_2O_2 \text{ transformed}} \quad (3)$$

4. Conclusions

The catalytic activities of the FeCo-based catalysts were assessed in the styrene oxidation to benzaldehyde, acetophenone, ethylbenzene, 2-phenyl ethanol, 2-phenyl acetic acid, 2-phenyl acetaldehyde, and styrene polymerization products. Among the various preparation methods used, namely, sol–gel, chemical modification, copolymer-assisted co-precipitation, and nanocasting, the nanocasting and chemical modification produced catalysts with a semi-crystalline structure and defined porosity, which in turn enhanced the formation of the desired products. The other methods allow for the synthesis of solids with low selectivities to the desired products. A considerable influence on the conversion and selectivity was observed when using Mo, Cu, or Sn. The tin nanoparticles dispersed in an FeCo matrix was added, affording a styrene conversion of styrene oxide greater than 70% and a selectivity of the desired products of more than 50%.

Acknowledgments: The authors are grateful for support from FUNCAP/CAPES and CNPq. A.P.S.O. recognizes financial support from CNPq scholarship. SEM-EDS studies were performed using facilities of Central Analítica da Universidade Federal do Ceará. This work was partially supported by the CETENE through TEM and isotherms measurements. We are grateful to A.S.B.N. for XRD discussions.

Author Contributions: A.P.S.O., I.S.G. and A.C. performed the experiments; A.C.O., J.M.S. and F.F.d.S. analyzed the data and wrote the manuscript; G.D.S. and J.M.F. designed the experiments.

Conflicts of Interest: The authors declare no conflict of interest.

References

1. Bedford, R.B. How Low Does Iron Go? Chasing the Active Species in Fe-Catalyzed Cross-Coupling Reactions. *Acc. Chem. Res.* **2015**, *48*, 1485–1493. [CrossRef] [PubMed]
2. Ali, M.E.; Rahman, M.M.; Sarkar, S.M.; Hamid, S.B.A. Heterogeneous Metal Catalysts for Oxidation Reactions. *J. Nanomater.* **2014**. [CrossRef]
3. Barona-Castaño, J.C.; Carmona-Vargas, C.C.; Brocksom, T.J.; de Oliveira, K.T. Porphyrins as Catalysts in Scalable Organic Reactions. *Molecules* **2016**, *21*, 310. [CrossRef] [PubMed]
4. Cruz, M.G.A.; Fernandes, F.A.N.; Oliveira, A.C.; Filho, J.M.; Oliveira, A.C.; Campos, A.F.; Padron-Hernandez, E.; Rodríguez-Castellón, E. Effect of the calcination temperatures of the Fe-based catalysts supported on polystyrene mesoporous carbon for FTS Synthesis. *Catal. Today* **2017**, *282*, 174–184. [CrossRef]
5. Westsson, E.; Koper, G.J.M. How to Determine the Core-Shell Nature in Bimetallic Catalyst Particles? *Catalysts* **2014**, *4*, 375–396. [CrossRef]
6. Stahl, A.; Wang, Z.; Schwämmle, T.; Ke, J.; Li, X. Novel Fe-W-Ce Mixed Oxide for the Selective Catalytic Reduction of NO_x with NH_3 at Low Temperatures. *Catalysts* **2017**, *7*, 71. [CrossRef]
7. Owens, G.J.; Singh, R.K.; Foroutan, F.; Alqaysi, M.; Han, C.-M.; Mahapatra, C.; Kim, H.-W.; Knowles, J.C. Sol–gel based materials for biomedical applications. *Prog. Mater. Sci.* **2016**, *77*, 1–79. [CrossRef]

8. Castro, A.J.R.; Marques, S.P.D.; Soares, J.M.; Filho, J.M.; Saraiva, G.D.; Oliveira, A.C. Nanosized aluminum derived oxides catalysts prepared with different methods for styrene production. *Chem. Eng. J.* **2012**, *209*, 345–355. [CrossRef]
9. Xia, L.Y.; Zhang, M.Q.; Yuana, C.; Rong, M.Z. A facile heteroaggregate-template route to hollow magnetic mesoporous spheres with tunable shell structures. *J. Mater. Chem.* **2011**, *21*, 9020–9026. [CrossRef]
10. Solsona, B.; García, T.; Sanchis, R.; Soriano, M.D.; Moreno, M.; Rodríguez-Castellón, E.; Agouram, S.; Dejoz, A.; López Nieto, J.M. Total oxidation of VOCs on mesoporous iron oxide catalysts: Soft chemistry route versus hard template method. *Chem. Eng. J.* **2016**, *290*, 273–281. [CrossRef]
11. Jahagirdar, A.A.; Dhananjaya, N.; Monika, D.L.; Kesavulu, C.R.; Nagabhushana, H.; Sharma, S.C.; Nagabhushana, B.M.; Shivakumara, C.; Rao, J.L.; Chakradhar, R.P.S. Structural, EPR, optical and magnetic properties of α-Fe_2O_3 nanoparticles. *Spectrochim. Acta Part A Mol. Biomol. Spectrosc.* **2013**, *104*, 512–551. [CrossRef] [PubMed]
12. Oliveira, A.P.S.; Gomes, I.S.; Neto, A.S.B.; Oliveira, A.C.; Filho, J.M.; Saraiva, G.D.; Soares, J.M.; Tehuacanero-Cuapa, S. Catalytic performance of MnFeSi composite in selective oxidation of styrene, ethylbenzene and benzyl alcohol. *Mol. Catal.* **2017**, *436*, 29–42. [CrossRef]
13. Brookes, C.; Bowker, M.; Wells, P.P. Catalysts for the Selective Oxidation of Methanol. *Catalysts* **2016**, *6*, 92. [CrossRef]
14. Wang, B.; Zhang, J.; Zou, X.; Dong, H.; Yao, P. Selective oxidation of styrene to 1,2-epoxyethylbenzene by hydrogen peroxide over heterogeneous phosphomolybdic acid supported on ionic liquid modified MCM-41. *Chem. Eng. J.* **2015**, *260*, 172–177. [CrossRef]
15. Ghosh, B.K.; Moitra, D.; Chandel, M.; Patra, M.K.; Vadera, S.R.; Ghosh, N.N. CuO Nanoparticle Immobilised Mesoporous TiO_2–Cobalt Ferrite Nanocatalyst: A Versatile, Magnetically Separable and Reusable Catalyst. *Catal. Lett.* **2017**, *147*, 1061–1076. [CrossRef]
16. Sun, J.; Yu, G.; Huo, Q.; Kan, Q.; Guan, J. Epoxidation of styrene over Fe(Cr)-MIL-101 metal-organic frameworks. *RSC Adv.* **2014**, *4*, 38048–38054. [CrossRef]
17. Neto, A.B.S.; Pinheiro, L.G.; Filho, J.M.; Oliveira, A.C. Studies on styrene selective oxidation over iron-based catalysts: Reaction parameters effects. *Fuel* **2015**, *150*, 305–317. [CrossRef]
18. Grasselli, R.K.; Centi, G.; Trifiro, F. Selective oxidation of hydrocarbons employing tellurium containing heterogeneous catalysts. *Appl. Catal.* **1990**, *57*, 149–166. [CrossRef]
19. Cruz, M.G.A.; Oliveira, A.P.S.; Fernandes, F.A.N.; Sousa, F.F.; Oliveira, A.C.; Filho, J.M.; Campos, A.F.; Rodríguez-Castellón, E. Fe-containing carbon obtained from ferrocene: Influence of the preparation procedure on the catalytic performance in FTS reaction. *Chem. Eng. J.* **2017**, *317*, 143–156. [CrossRef]
20. Marques, S.P.D.; Pinheiro, A.L.; Braga, T.P.; Valentini, A.; Filho, J.M.; Oliveira, A.C. Nanocasted oxides for oxidative dehydrogenation of ethylbenzene utilizing CO_2 as soft oxidant. *J. Mol. Catal. A Chem.* **2011**, *348*, 1–13. [CrossRef]
21. Park, C.; Jung, J.; Lee, C.W.; Chol, J. Synthesis of Mesoporous α-Fe_2O_3 Nanoparticles by Non-ionic Soft Template and Their Applications to Heavy Oil Upgrading. *Sci. Rep.* **2016**, *6*, 39136. [CrossRef] [PubMed]
22. Toki, M.; Chow, T.Y.; Ohnaka, T.; Samura, H.; Saegusa, T. Structure of poly(vinylpyrrolidone)-silica hybrid. *Polym. Bull.* **1992**, *29*, 653–660. [CrossRef]
23. Ma, Y.; Huang, Y.; Wang, X.; Jia, D.; Tang, X. One-pot synthesis of Fe_3O_4/C nanocomposites by PEG-assisted co-precipitation as anode materials for high-rate lithium-ion batteries. *J. Nanopart. Res.* **2014**, *16*, 2614–2616. [CrossRef]
24. Yin, M.; Hasier, J.; Nash, P. A review of phase equilibria in Heusler alloy systems containing Fe, Co or Ni. *J. Mater. Sci.* **2016**, *51*, 50–70. [CrossRef]
25. Malaman, B.; Le Caër, G.; Costa, B.F.O. B2 long-range order in mechanically alloyed $Fe_{53.3-0.6x}Co_{46.7-0.4x}Sn_x$ ($2 \leq x \leq 26$) annealed at moderate temperatures. *J. Mater. Sci.* **2016**, *51*, 5775–5790. [CrossRef]
26. Huang, Z.; Bensch, W.; Sigle, W.; van Aken, P.A.; Kienle, L.; Vitoya, T.; Modrow, H.; Ressler, T. The modification of MoO_3 nanoparticles supportedon mesoporous SBA-15: Characterization using X-ray scattering, N_2 physisorption, transmission electron microscopy, high-angleannular darkfield technique, Raman and XAFS spectroscopy. *J. Mater. Sci.* **2008**, *43*, 244–253. [CrossRef]
27. Casulam, M.F.; Corrias, A.; Falqui, A.; Serin, V.; Gatteschi, D.; Sangregorio, C.; Julián Fernández, C.; Battaglin, G. Characterization of FeCo–SiO_2 Nanocomposite Films Prepared by Sol–Gel Dip Coating. *Chem. Mater.* **2003**, *15*, 2201–2207. [CrossRef]

28. Leitner, A.; Sakeye, M.; Zimmerli, C.E.; Smått, J.-H. Insights into chemoselectivity principles in metal oxide affinity chromatography using tailored nanocast metal oxide microspheres and mass spectrometry-based phosphoproteomics. *Analyst* **2017**, *142*, 1993. [CrossRef] [PubMed]
29. Gao, F.; Li, Y.; Zhao, Y.; Wan, W.; Du, G.; Ren, X.; Zhao, H. Facile synthesis of flower-like hierarchical architecture of SnO_2 nanoarrays. *J. Alloys Compd.* **2017**, *703*, 354–360. [CrossRef]
30. Volanti, D.P.; Keyson, D.; Cavalcante, L.S.; Simoes, A.Z.; Joya, M.R.; Longo, E.; Varela, J.A.; Pizani, P.S.; Souza, A.G. Synthesis and characterization of CuO flower-nanostructure processing by a domestic hydrothermal microwave. *J. Alloys Compd.* **2008**, *459*, 537–542. [CrossRef]
31. Sharma, R.K.; Reddy, G.B. Synthesis and characterization of α-MoO_3 microspheres packed with nanoflakes. *J. Phys. D Appl. Phys.* **2014**, *47*, 065305. [CrossRef]
32. Jnaneshwaraetal, D.M.; Avadhan, D.N.; Prasad, B.D.; Nagabhushana, B.M.; Nagabhushan, H.; Sharma, S.C.; Shivakuma, C.; Rao, J.L.; Gopal, N.O.; Chakradhar, K.R.P.S. Electron paramagnetic resonance, magnetic and electrical properties of $CoFe_2O_4$ nanoparticles. *J. Magn. Magn. Mater.* **2013**, *339*, 40–45. [CrossRef]
33. Misra, S.K.; Andronenko, S.I. Magnetic resonance studies of Co^{2+} ions in nanoparticles of SnO_2 processed at different temperatures. *J. Appl. Phys.* **2006**, *99*, 08M106. [CrossRef]
34. Langhammer, H.T.; Böttcher, R.; Müller, T.; Walther, T.; Ebbinghaus, S.G. Defect properties of cobalt-doped hexagonal barium titanate ceramics. *J. Phys. Condens. Matter.* **2015**, *27*, 295901. [CrossRef] [PubMed]
35. Silva, L.A.; Andrade, J.B.; Mangrich, A.S. Use of Cu^{2+} as a metal ion probe for the EPR study of metal complexation sites in the double sulfite CuI_2SO_3.CdIISO_3 $2H_2O$. *J. Braz. Chem. Soc.* **2007**, *18*, 607–610. [CrossRef]
36. Agarwal, A.; Khas, S.; Sanghi, S.; Seth, V.P.; Arora, M. Effect of MoO_3 on electron paramagnetic resonance spectra, optical spectra and dc conductivity of vanadyl ion doped alkali molybdo-borate glasses. *J. Mol. Struct.* **2014**, *1060*, 182–190. [CrossRef]
37. Jiang, T.; Poyraz, A.S.; Iyer, A.; Zhang, Y.; Lu, Z.; Zhong, W.; Miao, R.; El-Sawy, A.M.; Guild, C.J.; Sun, Y.D.; et al. Synthesis of mesoporous iron oxides by an inverse micelle, ethod and their application in the degradation of orange II under visible light at neutral pH. *J. Phys. Chem. C* **2015**, *119*, 10454–10468. [CrossRef]
38. Zhang, Y.; Li, Z.; Sun, W.; Xi, C. A magnetically recyclable heterogeneous catalyst: Cobalt nano-oxide supported on hydroxyapatite-encapsulated γ-Fe_2O_3 nanocrystallites for highly efficient olefin oxidation with H_2O_2. *Catal. Commun.* **2008**, *10*, 237–242. [CrossRef]
39. Li, M.; Wu, S.; Yang, X.; Hu, J.; Peng, L.; Bai, L.; Huo, Q.; Guan, J. A Highly efficient single atom cobalt catalyst for selective oxidation of alcohols. *Appl. Catal. A Gen.* **2017**, *543*, 61–66. [CrossRef]
40. Wang, Y.; Zhao, H.; Zhao, G. Iron-copper bimetallic nanoparticles embedded within ordered mesoporous carbon as effective and stable heterogeneous Fenton catalyst for the degradation of organic contaminants. *Appl. Catal. B Environ.* **2015**, *164*, 396–406. [CrossRef]
41. Arcibar-Orozco, J.A.; Giannakoudakis, D.A.; Bandosz, T.J. Effect of Ag containing (nano)particles on reactive adsorption of mustard gas surrogate on iron oxyhydroxide/graphite oxide composites under visible light irradiation. *Chem. Eng. J.* **2017**, *303*, 123–136. [CrossRef]
42. Krishnankutty, N.; Rodriguez, N.M.; Baker, R.T.K. Effect of Copper on the Decomposition of Ethylene over an Iron Catalyst. *J. Catal.* **1996**, *158*, 217–227. [CrossRef]
43. Kameoka, S.; Tanabe, T.; Tsai, A.P. Spinel $CuFe_2O_4$: A precursor for copper catalyst with high thermal stability and activity. *Catal. Lett.* **2005**, *100*, 89–93. [CrossRef]
44. Florent, M.; Giannakoudakis, D.A.; Wallace, R.; Bandosz, T.J. Mixed CuFe and ZnFe (hydr)oxides as reactive adsorbents of chemicalwarfare agent surrogates. *J. Hazard. Mater.* **2017**, *329*, 141–145. [CrossRef] [PubMed]
45. Wallace, R.; Florent, M.; Karwacki, C.J.; Bandosz, T.J. Ferrihydrite deposited on cotton textiles as protection media against the chemical warfare agent surrogate (2-chloroethyl ethyl sulfide). *J. Mater. Chem. A* **2017**, *5*, 4972. [CrossRef]
46. Kyzas, G.Z.; Deliyanni, E.A.; Bele, S.I.; Matis, K.A. Nano-Adsorbent for Arsenates: Iron Oxyhydroxide Impregnated Microporous Activated Carbon. *Curr. Environ. Eng.* **2014**, *1*, 51–58. [CrossRef]
47. Dabbawala, A.A.; Sudheesh, N.; Bajaj, H.C. Palladium supported on chitosan as a recyclable and selective catalyst for the synthesis of 2-phenyl ethanol. *Dalton Trans.* **2012**, *41*, 2910–2917. [CrossRef] [PubMed]
48. Miller, A.A.; Mayn, F.R. Oxidation of Unsaturated Compounds. I. The Oxidation of Styrene. *J. Am. Chem. Soc.* **1956**, *78*, 1017–1023. [CrossRef]

49. Perandones, B.F.; del Rio Nieto, E.; Godard, C.; Castillon, S.; De Frutos, P.; Claver, C. Fe-Catalyzed Olefin Epoxidation with Tridentate Non- Heme Ligands and Hydrogen Peroxide as the Oxidant. *ChemCatChem* **2016**, *8*, 2930–2938.
50. Pomogailo, A.D. *Catalysis by Polymer-Immobilized Metal Complexes*; CRC Press: Boca Raton, FL, USA, 1999; pp. 1–424.
51. 51 Maurya, M.R.; Kumar, N. Sodium bicarbonate assisted oxidation, by H_2O_2, of styrene and cyclohexene using polymer grafted dioxidomolybdenum(VI) complex as a catalyst. *J. Mol. Catal. A Chem.* **2015**, *406*, 204–212. [CrossRef]